

1 This is a manuscript is a **preprint** and has been submitted to **Tectonics**. This manuscript has not undergone  
2 peer-review. Subsequent versions of the manuscript may have different content. If accepted, the final  
3 version of this manuscript will be available via the “Peer-reviewed Publication” DOI link on the right-hand  
4 side of this webpage. Please feel free to contact any of the authors directly to comment on the manuscript.

5

6                                    **The kinematics of growth faults and the role of lateral tip retreat**

7

8    **Bailey A. Lathrop<sup>1</sup>, Christopher A.-L. Jackson<sup>1</sup>, Rebecca E. Bell<sup>1</sup>, Atle Rotevatn<sup>2</sup>**

9    <sup>1</sup> Basins Research Group (BRG), Department of Earth Science & Engineering, Imperial College,

10 Prince Consort Road, London, SW7 2BP, UK

11 <sup>2</sup> Department of Earth Science, University of Bergen, PO Box 7800, 5020 Bergen, Norway

12

13 Corresponding author: Bailey Lathrop (b.lathrop17@imperial.ac.uk)

14

15    **Key Points:**

- 16            • We document normal fault growth in the Exmouth Plateau, Offshore Australia
- 17            • Faults follow a three stage growth model: lengthening stage, throw accumulation stage,
- 18            tip retreat stage
- 19            • We suggest that tip retreat could be an important stage of normal fault growth

20

## 21 **Abstract**

22 Understanding how normal faults grow is key to determining the tectono-stratigraphic evolution  
23 of rifts and the distribution and size of potentially hazardous earthquakes. According to recent  
24 studies, normal faults tend to grow in two temporally distinct stages: a lengthening stage,  
25 followed by a throw/displacement accumulation stage. However, this model is still debated and  
26 not widely supported by many additional studies. Relatively few studies have investigated what  
27 happens to a fault as it becomes inactive, i.e. does it abruptly die, or does its at-surface trace-  
28 length progressively shorten by so-called tip retreat? We here use a 3D seismic reflection dataset  
29 from the Exmouth Plateau, offshore Australia to develop a three-stage fault growth model for  
30 seven normal faults of various sizes, and to show how the throw-length scaling relationship  
31 changes as a fault dies. We show that during the lengthening stage, which lasted <30% of the  
32 faults life, faults reached their near-maximum lengths, yet accumulated only 10-20% of their  
33 total throw. During the throw/displacement accumulation stage, which accounts for c. 30-75% of  
34 the faults life, throw continued to accumulate along the entire length of the faults. All of the  
35 studied faults also underwent a stage of lateral tip-retreat (last c. 25% of the faults lives), where  
36 the active at-surface trace-length decreased by up to 25%. This work has implications for our  
37 understanding of the temporal evolution of normal faults, in particular how they grow and how  
38 they die, with the final stage of tip retreat typically being absent from more fault growth models.

## 39 **1 Introduction**

40 Normal fault growth models have been widely debated over the past c. 20 years. The  
41 propagating fault model, also referred to as the isolated fault model (Walsh et al., 2003), suggests  
42 that normal faults grow via a synchronous increase in length and displacement, i.e. that when  
43 faults lengthen they also accumulate displacement. Faults can also lengthen via tip propagation

44 and linkage of these individual segments (e.g. Cartwright et al., 1995; Dawers et al., 1993;  
45 Morley et al., 1990; Walsh et al., 2003; Walsh & Watterson, 1988). The constant-length model  
46 instead suggests that normal faults reach their near-final lengths relatively rapidly and spend the  
47 rest of their lives accruing displacement without further significant lengthening (Childs et al.,  
48 2017; Fossen & Rotevatn, 2016; Hemelsdaël & Ford, 2016; Henstra et al., 2015; Jackson and  
49 Rotevatn, 2013; Nicol et al., 2005, 2016; Tvedt et al., 2016; Walsh et al., 2002, 2003; see also  
50 Cowie et al., 1998). However, Jackson et al. (2017) and Rotevatn et al. (2019) propose that the  
51 propagating fault model and the constant-length models may not in fact be mutually exclusive,  
52 end-member models, but instead represent discrete kinematic phases in the life of a single fault.  
53 The hybrid growth model combines both and states that faults grow in two stages: the  
54 lengthening stage (propagating fault stage) and the displacement accrual stage (constant-length  
55 stage) (Jackson et al., 2017; Rotevatn et al., 2019). According to the hybrid model proposed by  
56 Rotevatn et al., (2019), during the lengthening stage, which encompasses c. 20-30% of the  
57 duration of a faults life, faults reach their near-final length via the propagation and linkage of  
58 relatively small, discrete segments; during this time, the fault accumulates 10-60% of its total  
59 displacement. During the displacement accrual stage, which takes place during the latter 70-80%  
60 of the faults life, the fault accumulates 40-90% of its total displacement (Jackson et al., 2017;  
61 Rotevatn et al., 2019). Examples of normal faults with preserved, seismically well-imaged  
62 growth strata to provide reliable kinematic constraints on fault growth are rare, thus the hybrid  
63 growth model (and the component propagating and constant-length stages) has only rarely been  
64 tested. Such tests are needed if we are to fully understand normal fault growth.

65         Whereas many studies have investigated how normal faults initiate and grow (see above),  
66 few have considered what happens at the end of a faults life. These few studies propose that

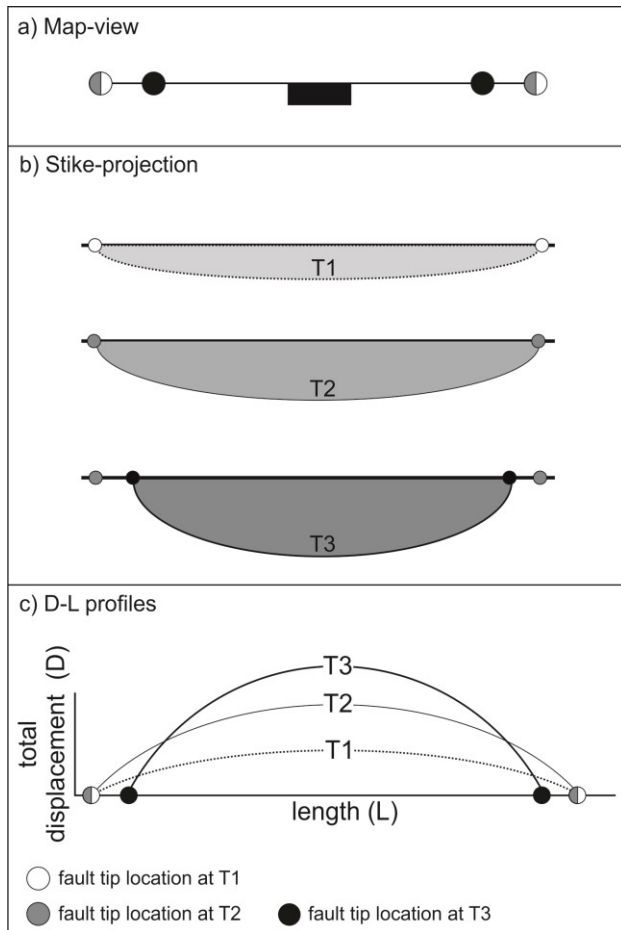
67 faults die in two general ways: the entire trace-length of the fault remains active before slip  
68 ceases, or that, as the fault dies, activity is focused onto the centre of the fault, leading to a  
69 progressively shorter active fault trace-length (Childs et al., 2003; Meyer et al., 2002). In the  
70 latter case, normal faults experience a stage of fault tip retreat, i.e., the lateral tip regions do not  
71 accumulate further displacement or throw as strain is localized near the fault centre (Figure 1;  
72 Meyer et al., 2002). In 3D seismic reflection data, tip retreat can be observed by identifying  
73 packages of growth strata that are deposited over progressively shorter along-strike lengths as the  
74 fault reaches the end of its life (Meyer et al., 2002). Tip retreat has also been interpreted as a  
75 result of relay breaching during segment linkage (Childs et al., 2003); however, this is not the  
76 style of tip retreat we identify in this study.

77         Relatively few studies have discussed the role tip retreat plays in the evolution of normal  
78 faults (Childs et al., 2003; Freitag et al., 2017; Meyer et al., 2002; Morley, 2002), and it is  
79 therefore not usually included in fault growth models. This likely reflects the fact it is very  
80 difficult or sometimes impossible to constrain the kinematics of normal faults, for example in  
81 cases where growth strata are absent and/or only locally preserved. To the best of our  
82 knowledge, tip retreat has also not yet been the focus of or identified in, physical or numerical  
83 models. Freitag et al., (2017) show an example of tip retreat in the Columbus Basin, offshore  
84 Trinidad; these are, however, thin-skinned, gravity-driven faults, and it is not clear if the  
85 kinematics would apply to thick-skinned faults offsetting crystalline basement. Morley (2002)  
86 also show an example of possible tip retreat in the East African Rift, but since this is a sediment-  
87 starved (i.e. underfilled) basin, it is difficult to tell if the fault really experienced tip retreat, or  
88 whether the observed geometries simply reflect post-fault death passive filling of hanging wall  
89 accommodation. We seek to provide the first well-constrained examples of tip retreat occurring

90 on basement-involved normal faults, as well as guidance on how to identify this important  
91 process in the rock record.

92         In this paper, we use 3D seismic reflection and borehole data from the Exmouth Plateau,  
93 offshore Australia to study the kinematics of basement-involved normal faults. More specifically  
94 we: 1) constrain the temporal relationship between fault lengthening and displacement; and 2)  
95 investigate the role of tip retreat as faults become inactive. This is an excellent place to study this  
96 process because synsedimentary normal faults are well-preserved, age-constrained, and well-  
97 imaged in excellent-quality, open-source, 3D seismic reflection data. The rift basin was also  
98 overfilled for much of the duration of faulting, meaning the faults are flanked by well-developed  
99 growth (syn-tectonic) strata.

100



101

102 **Figure 1.** Conceptual models for the development of normal faults following a “hybrid fault  
 103 model” (Rotevatn et al., 2019) with a stage of tip retreat. Time 1 (T1) represents the  
 104 lengthening/propagating fault model stage, Time 2 (T2) represents the displacement  
 105 accumulation/constant-length model stage, and Time 3 (T3) represents a phase of fault tip-line  
 106 retreat. **a)** map view of the active fault trace line at T1-3. Note that the fault reaches its maximum  
 107 length at T1, and has a shorted active trace line at T3. **b)** along-strike projection of throw at T1-3.  
 108 An increasing amount of displacement is accumulated at each stage. **c)** Displacement/length  
 109 profile at T1-3.

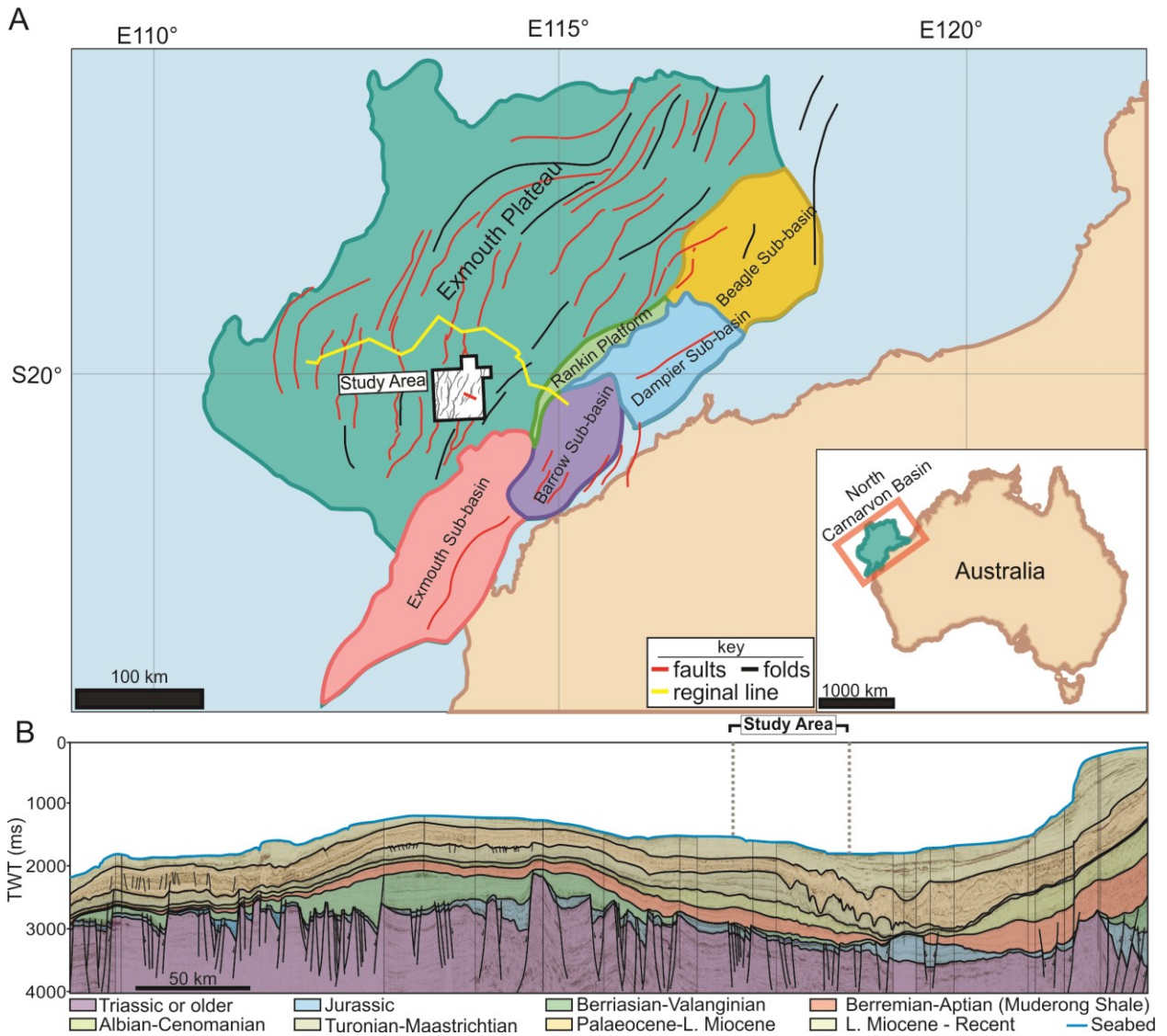
110 **2 Geologic setting of the Exmouth Plateau**

111 Our study area is located on the Exmouth Plateau, North Carnarvon Basin, offshore NW  
 112 Australia (Figure 2). The North Carnarvon Basin formed due to rifting in the Late  
 113 Carboniferous-Permian as a result of the breakup of Pangea, and the Exmouth Plateau formed as  
 114 a result of rifting between Greater India and Australia, creating NE-trending blocks (Gibbons et  
 115 al., 2012; Longley et al., 2002; Stagg & Colwell, 1994). The Exmouth Plateau is located in the

116 northern part of the North Carnarvon Basin, bounded by the continental shelf to the southeast,  
117 and the Curvier, Gascoyne, and Argo abyssal plains to the SW, SW, and NE, respectively  
118 (Longley et al., 2002). The Exmouth Plateau is a block of thin crystalline crust, and based on  
119 geophysical evidence, it has been suggested that the Exmouth Plateau basement is continental  
120 crust, however this has not been confirmed by direct sampling (Stagg et al., 2004). The  
121 crystalline basement is overlain by a thick pre-rift succession, consisting of the fluvial-deltaic to  
122 marginal marine, Mungaroo Formation (Triassic) (Longley et al., 2002; Stagg et al., 2004).

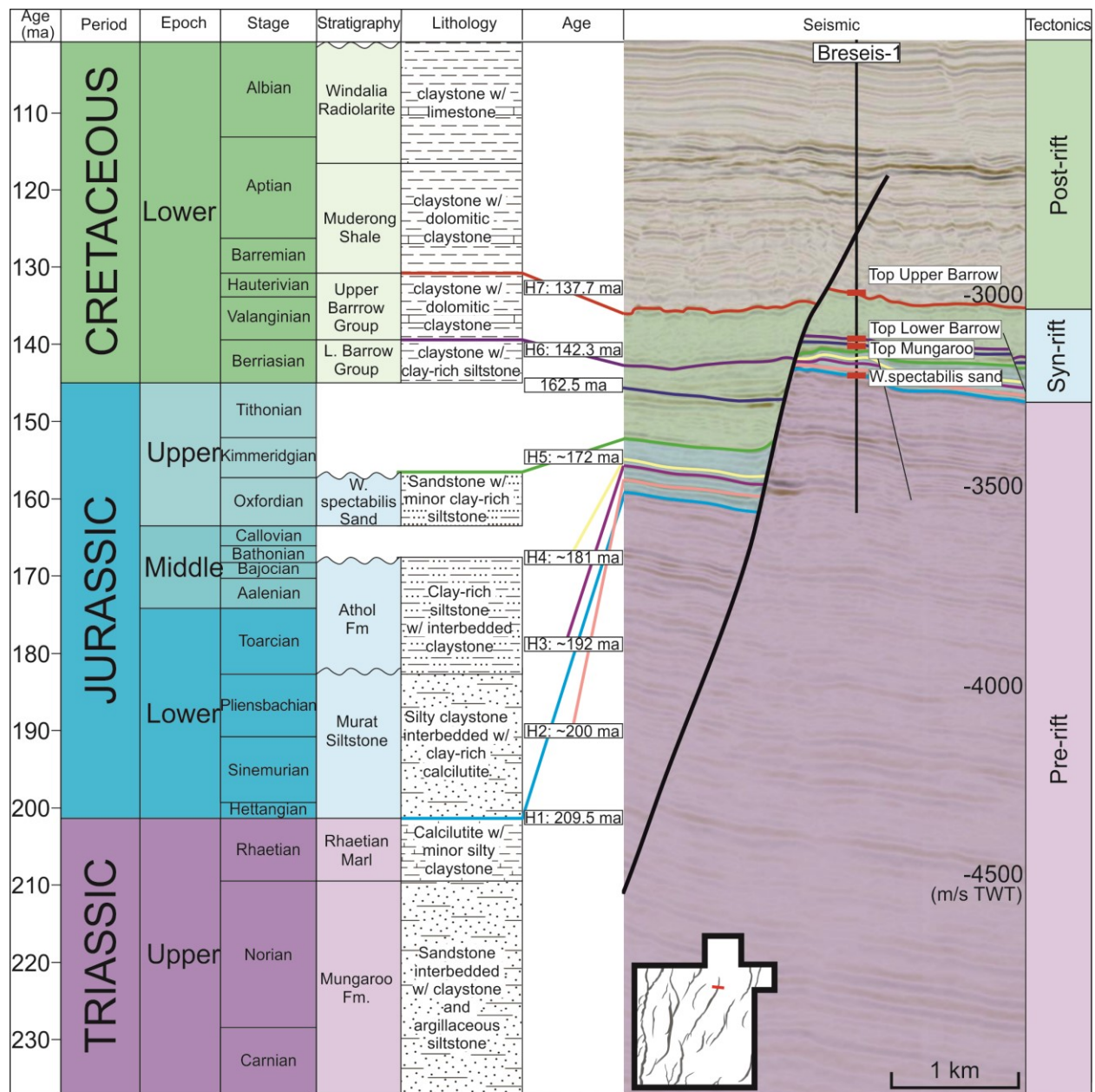
123         The synrift extension began in the Late Triassic (Rhaetian) until Late Jurassic  
124 (Oxfordian), during which time the Murat and Athnol siltstones were deposited in a sediment-  
125 starved basin (Figure 3) (Longley et al., 2002; Tindale et al., 1998). After a short period of  
126 tectonic quiescence in the Late Jurassic, rifting continued in the Early Cretaceous in an over-  
127 filled basin environment, during which time marine claystones (Dingo Claystone) and coarser-  
128 grained, deltaic clastics (Barrow Group) were deposited (Longley et al., 2002). Rifting in the  
129 Exmouth Plateau ceased in the Hauterivian, and the area became a passive margin (Gibbons et  
130 al., 2012; Longley et al., 2002). In this paper, we focus on the Jurassic-Early Cretaceous, syn-  
131 sedimentary normal faults which are generally trending N- NE.





132  
133  
134  
135

**Figure 2.** Study area **a)** location of the Exmouth Plateau in the North Carnarvon Basin, offshore Australia. Structural details based off of Pan et al., (2020), **b)** Regional 2D seismic line across the study area, modified from Nugraha et al., (2019).



136  
 137 **Figure 3.** Stratigraphic framework showing the key interpreted seismic horizons, their ages, and  
 138 the tectonic evolution of the Exmouth Plateau (H=horizon). Ages for H1, H5, H6, and H7 were  
 139 taken from Marshal and Lang (2013), and H2, H3, and H4 are relative dates assuming constant  
 140 sedimentation. Information on the tectonostratigraphic framework are from Bilil et al., (2018)  
 141 and Geoscience Australia.

## 142 **3 Data**

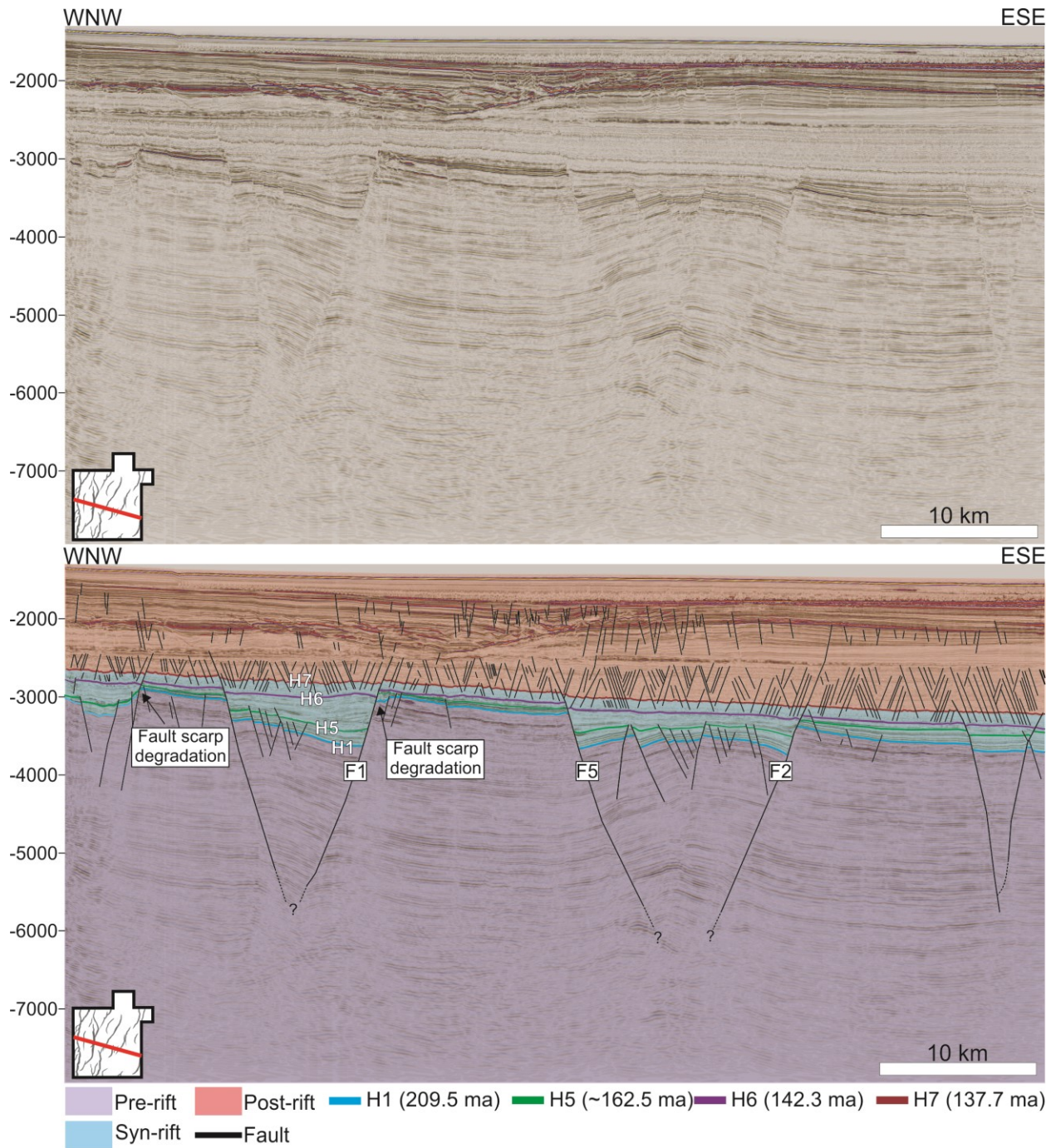
### 143 **3.1 Data**

144 The Glencoe dataset is a 3D time-migrated seismic reflection survey that encompasses  
145 approximately 3900 km<sup>2</sup> of the Kangaroo syncline in the Exmouth Plateau (Figure 4). It has a  
146 bin spacing of 25 m and a record length of 8 s two-way time (TWT). The vertical and horizontal  
147 resolution are approximated by a quarter of the dominant wavelength of the data, yielding c. 6.6  
148 m ( $\lambda=26.3$  m) within the syn-rift sediments (Brown, 2011). Seismic sections are displayed with  
149 normal polarity (SEG European Convention; Brown, 2011), where increase in acoustic  
150 impedance is represented by a peak (red), and an decrease by a trough (black). Seismic inlines  
151 are orientated WNW-ESE and the survey is tied to four wells (Glencoe-1, Nimblefoot-1,  
152 Warrior-1, and Breseis-1). Well-logs, formation tops, and biostratigraphic ages were provided  
153 with the wells. All seismic and well data are open-access and available from Geoscience  
154 Australia.

155 We have mapped seven regionally extensive seismic horizons (H1-7); H1, H6, and H7  
156 are age-constrained well-tied horizons with ages from well reports, as well as ages obtained by  
157 Marshall & Lang (2013) using biostratigraphy from 1500 wells around the North Carnarvon  
158 Basin (Figure 3). We lack direct age-constraints for H2-5, thus we estimated their ages by  
159 assuming a constant sedimentation rate between horizons of known ages (Figure 3). We also  
160 locally picked additional horizons within the syn-sedimentary deposits (e.g. H5.5) that are not  
161 continuous across the entire dataset; we estimated their ages based on an assumption of constant  
162 sedimentation rates between overlying and underlying, age-constrained horizons. We mapped  
163 and analyzed seven faults of varying sizes (8.8-42 km long, with 165-680 m of throw) to show

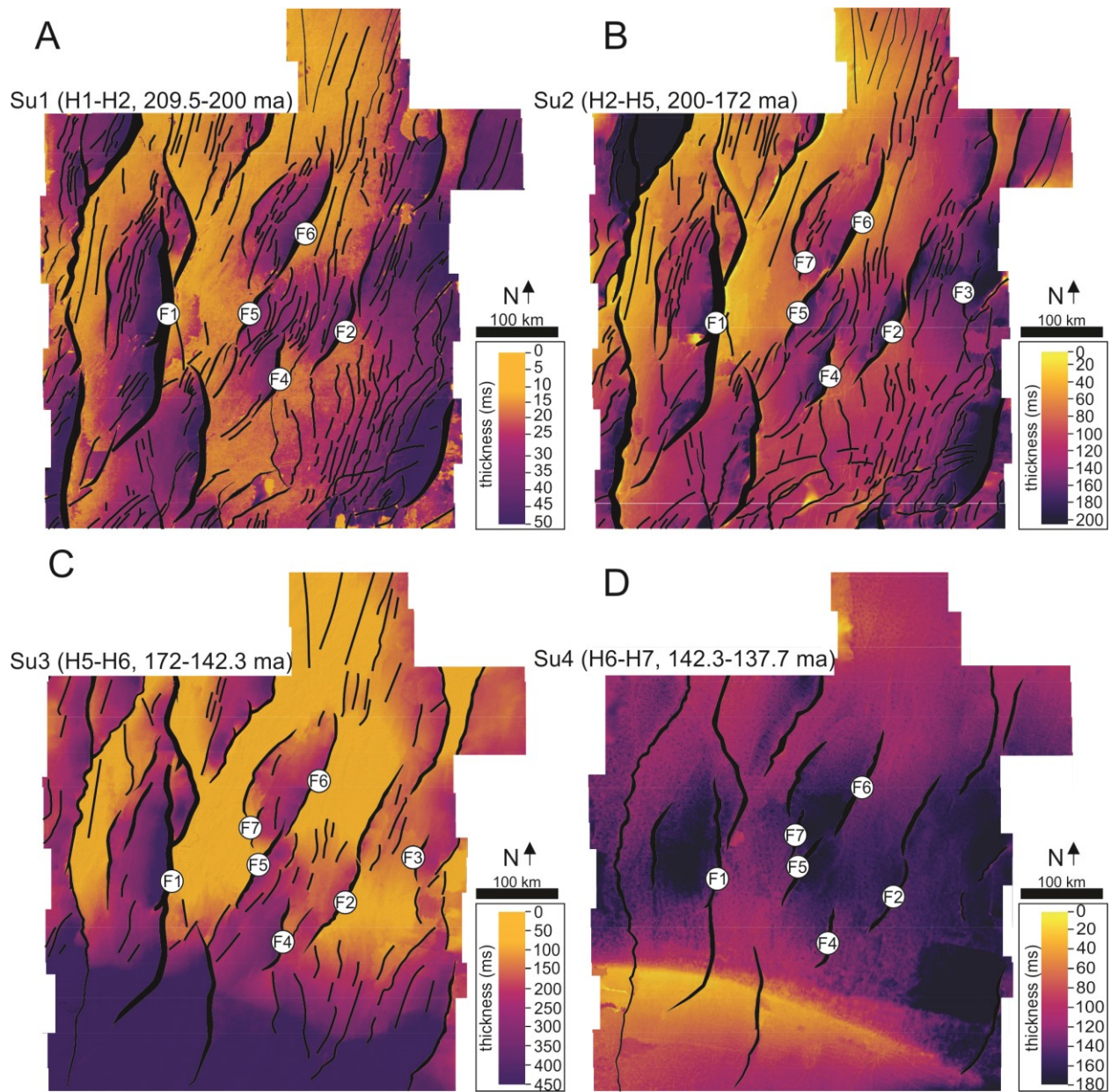


164 how faults of different sizes grow in the area, and to see if the styles of fault growth are scale  
 165 dependent (see Figure 5 for fault locations).



166

167 **Figure 4.** Representative seismic line in TWT across the central section of the 3D dataset, along  
 168 strike of the studied faults. Data is show with and without interpretation.



169

170 **Figure 5.** Representative isochrons of the study area with interpreted major and minor faults  
 171 labeled. **a)** Seismic Unit 1: Horizon 1-2, 209.5-196 ma, **b)** Seismic Unit 2: Horizon 2-5, 196-  
 172 162.5 ma, **c)** Seismic Unit 3, Horizon 5-6. 162.5-142.3 ma , **d)** Seismic Unit 4, horizon 6-7.  
 173 142.3-137.7 ma.

174 **3.2 Methodology**

175 In this study we used four different methods to quantify fault growth: isochron analysis,  
 176 throw backstripping, and expansion index (EI) analysis (see review by Jackson et al. 2017). First,



177 we created time-thickness (isochron) maps of key stratigraphic intervals, which illustrate  
178 variations in sediment thickness. This highlights across-fault hanging wall thickening, which can  
179 reveal the growth history of a fault (e.g. Jackson & Rotevatn, 2013). Isochron analysis was done  
180 first in order to establish the general style of fault growth (i.e. a propagating, constant-length, or  
181 hybrid fault growth model), and then we conducted throw backstripping to be able to see exact  
182 fault throw and length through time in the faults life (Jackson et al., 2017). To begin throw  
183 backstripping, we created throw-length (T-x) plots by picking the hanging wall and footwall  
184 cutoffs for every chosen horizon across the length of the faults (appendix figures 1-3). In the case  
185 of folding or erosion (Figure 4), horizons used to calculate throw were projected across the fold  
186 or eroded fault scarp (e.g. Wilson et al., 2013). Throw backstripping involves subtracting the  
187 throw of a shallower horizon directly from the throw of a deeper horizon at the same along-strike  
188 position, with this being repeated for successively deeper horizons (Chapman & Meneilly, 1991;  
189 Peterson et al., 1992). We opted to use the “original method” of throw backstripping, where  
190 throw across different horizons is simply subtracted, as we did not want to make any  
191 assumptions about the style of fault growth (see Jackson et al., 2017 for more details on fault  
192 displacement backstripping methods). Finally, we used EI analysis to measure variations in  
193 stratal thickness across the fault by dividing the thickness of hanging wall stratal unit by that of  
194 the equivalent unit in the footwall (Bouroullec et al., 2004; Cartwright et al., 1998; Jackson et al.,  
195 2017; Thorsen, 1963) (See appendix figure 4). This technique shows the formation and growth of  
196 depocenters, and therefore how the faults lengthened (Jackson & Rotevatn, 2013).

197 We also calculated vertical throw gradients by dividing the change in throw by the  
198 change in depth of the shallowest two horizons offset across the fault. We calculated upper-tip  
199 throw gradients in order to demonstrate that the top of the fault was interacting with the free

200 surface rather than acting as a blind fault; this is important when trying to understand if faults  
201 experienced real tip-line retreat or not (Childs et al., 2003; Walsh & Watterson, 1988). Finally,  
202 we calculated fault slip rates by dividing displacement for a particular time period by the  
203 duration of that time period; this was done in order to investigate whether slip rates varied  
204 between the different stages of fault growth.

205         Since the basin was sediment-starved from the Early Jurassic until the Late Jurassic, as  
206 evidenced by the fault scarp degradation until the deposition of H5 (Figures 4, 6a, and 8a), our  
207 fault lengthening calculations are upper limit estimations. For example, if active faulting created  
208 hanging wall accommodation but the basin was sediment starved, this accommodation would  
209 have remained unfilled. Thus, what looks like tip propagation could just be prolonged filling of  
210 the hanging wall of an inactive normal fault (see Jackson et al., 2017). It is therefore possible that  
211 the faults reached their maximum lengths even quicker than what we estimate.

212         We use checkshot (velocity) data from our four wells to convert throw values from  
213 milliseconds two-way time (ms TWT) to depth (m) (see appendix figure 5). Throw values are  
214 presented in metres. Burial-related compaction of sedimentary rocks can result in throw  
215 calculations being underestimated, especially when rocks have a high shale content or are deeply  
216 buried (>2 km; see Taylor et al., 2008). Decompaction typically decreases throw estimates by  
217 <20% (Taylor et al., 2008), so we here give all throw and slip rate values an error to account for  
218 maximum of 20% decompaction.

## 219 **4 Results**

220         We have completed a comprehensive geometric and kinematic analysis of seven faults of  
221 various sizes (appendix figures 1-4). We first provide a detailed description of the geometry of  
222 three faults (and their related growth strata) that are representative of the various fault sizes

223 identified in the study area, before describing their kinematics. Fault 1 (F1) represents the largest  
224 studied fault, Fault 2 (F2) represents a mid-sized fault, and Fault 3 (F3) represents the smallest  
225 studied fault in the dataset. We then present and discuss the results for all of the studied faults.

## 226 **4.1 Fault 1**

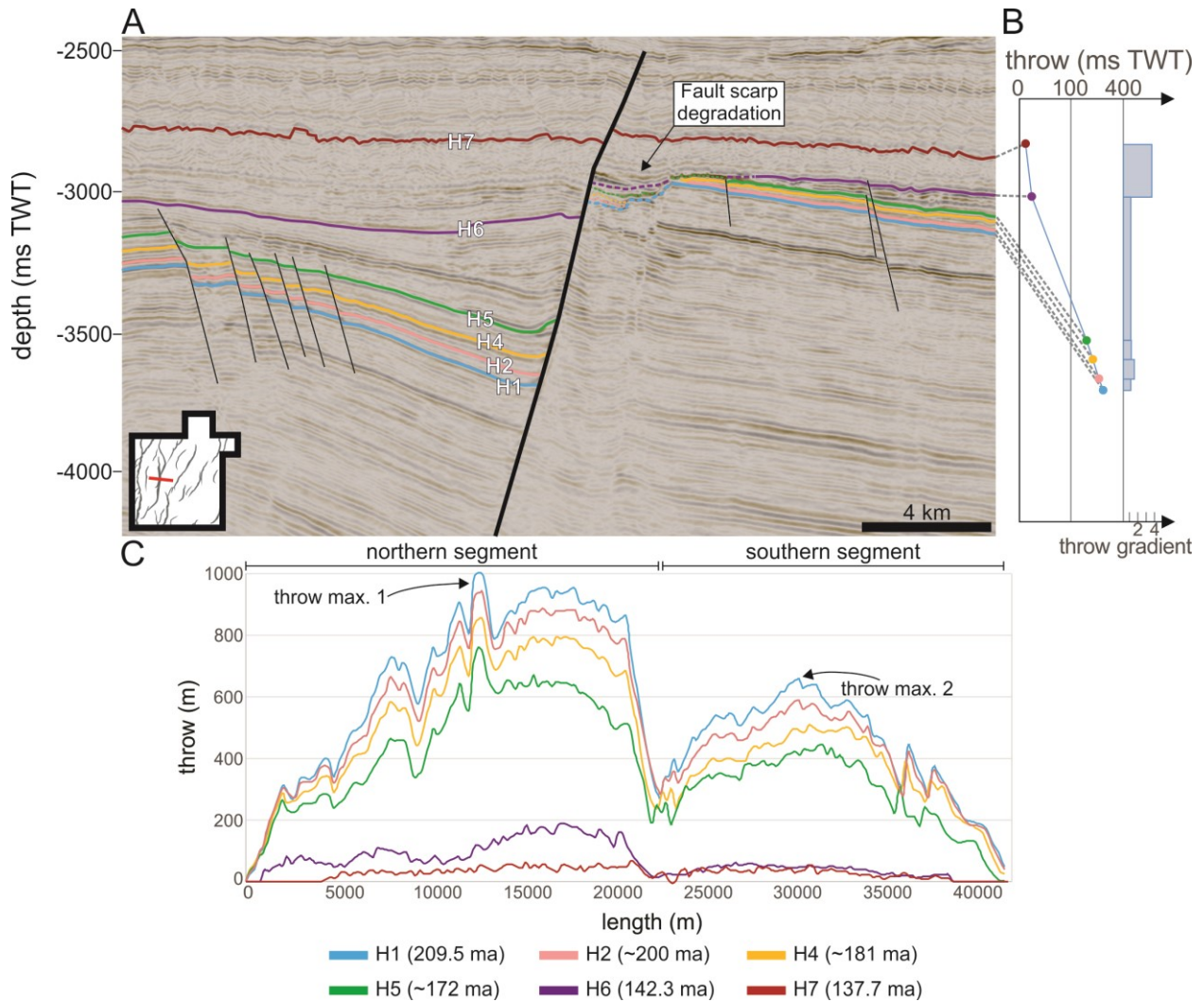
### 227 **4.1.1 Observations:**

228 Fault 1 (F1), the largest fault in the dataset that has both of its tips imaged, it is ~42 km  
229 long, strikes N-S, and dips to the E. Based on along-strike changes in strike and throw (Figure  
230 6c), we split F1 into a 24 km-long northern segment and an ~18 km-long southern segment  
231 (Figures 5 and 6). The upper tip-line of F1 is located in Lower Cretaceous strata, where it  
232 physically links to a tier of polygonal faults (Velayatham et al., 2019) (Figure 4), and its lower  
233 tip-line is difficult to locate due to poor seismic imaging in the pre-rift, but F1 appears to tip out  
234 deep in the study area or into the basement (Figure 4). F1 shows two clear throw maxima; a  
235 northern maximum (680 ms TWT <sup>{+136}</sup> or 1000 m <sup>{+200}</sup> at H1; error shows possible  
236 decompaction) near the centre of the northern fault segment, and a southern maximum (433 ms  
237 TWT <sup>{+87}</sup>, 658 m <sup>{+132}</sup> at H1) near the centre of the southern fault segment. Both segments are  
238 generally characterised by approximately bell-shaped throw distributions, the peak of which is  
239 skewed away from the center due to the related throw maxima being offset from the fault  
240 segment centres (Figure 6c).

241 There are clear wedge-shaped stratigraphic packages between H1 and H7 in the hanging  
242 wall; these thicken towards F1. In contrast, pre-H1 and post-H7 strata are isopachous (Figure  
243 6a). EI plots show across-fault thickening (i.e. values  $\geq 1$ ) in Unit 1 along the central parts of the  
244 northern and southern segments; the unit is, however, isopachous where the two segments link



245 (Figure 7a). In contrast, EI values in Unit 2 are  $\geq 1$  across the link between the two segments  
 246 (Figure 7b). EI values are  $\geq 1$  across a progressively longer portion of the fault in Units 2-5  
 247 (Figures 7b-d), until the youngest interval, Unit 6 (Figure 7e), where the upper tip of the fault is  
 248 associated with EI values  $< 1$ .



249

250 **Figure 6. a)** seismic profile illustrating F9 at its point of highest throw and its correlated throws  
 251 and throw gradients, **b)** throw-distance plot illustrating the lateral variations in throw across each  
 252 seismic unit. All throw values should be considered to be possible +20% due to decompaction  
 253 (Taylor et al., 2008).

254

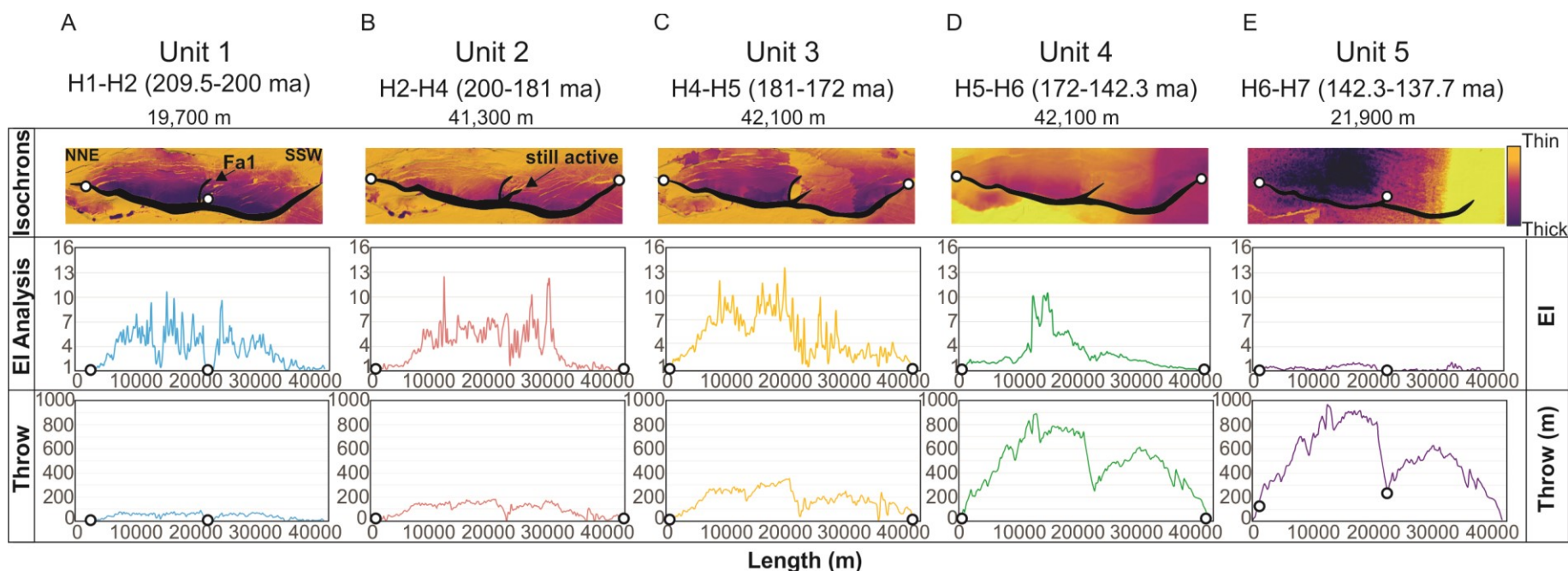


**Figure 7.** Isochrons, expansion index analysis, and throw throughout different stages of the life of Fault 1. The throw through time values are taken from displacement backstripping, which can be seen in detail in the appendix figures. White dots indicate the length of the fault at the specified interval. **a)** Isochron showing the thickness between H1 (209.5 my) and H2 (196 my), maximum throw is 78 m, and length is 19,700m, **b)** Isochron showing the thickness between H2 (196 my) and H4 (170 my), maximum throw is 191 m and length is 41,300 m, **c)** Isochron showing the thickness between H4 (170 my) and H5(162.5 my), maximum throw is 438 m and length is 41,100, **d)** Isochron showing the thickness between H5 (162.5 my) and H6 (142.3 my), maximum throw is 993 m and length is 42,100, **e)** Isochron showing the thickness between H6 (142.3 my) and H7 (137.7 my), maximum throw is 1098 and length is 21,900 m. All throw values should be considered to be possible +20% due to decompaction (Taylor et al., 2008).

#### 4.1.2 Interpretations:

We see across-fault thickening in the hanging wall between H1 and H7 (Units 1-5) in cross section (Figure 6a) and in isochron thickness maps (Figure 7a-e), suggesting F1 was active from 209.5 to 137.7 Ma (Early Jurassic-Early Cretaceous). In detail, however, the EI plots show that different parts of the fault were active at different times. The fact that F1 is associated with two discrete throw maxima (and two associated bell-shaped throw distributions), as well as an EI of  $<1$  in the middle of the fault in the first time interval (Unit 1; Figure 7a), suggests it formed by the linkage of two, initially separate segments. Linkage likely occurred some time between the deposition of H2 and H4, based on EI values of  $>1$  only occurring in units above H1. Often, when faults link, their paleo-tip-lines become inactive (Childs et al., 2003). In this case, however, F1 is a footwall-breached relay and the tip of the northern segment continued to accrue displacement on portions of the fault tips bounding the now-breached relay ramp (Figure 7e). The lack of throw in the middle of the fault is likely due to the still-active northern segment paleo-fault tip accommodating strain in the middle of the fault, as well as a minor E-W fault (labeled F1a in Figure 7a) that cuts perpendicularly across F1. F1 reached its maximum length by the deposition of H5 (Unit 3), or possibly sooner, based on the observation of EI values  $\geq 1$  across its length for this interval (Figure 7c). During Unit 5, the lateral ends of the fault have an EI value of  $<1$ , which suggests that the fault tips became inactive at this time. Additionally, during this last stage of fault growth, the breached relay ramp between the northern and southern segment had an EI value of  $<1$ , which suggests that the fault along the previously active relay ramp between the two fault segments became inactive (Figure 6e).

In summary, according to throw backstripping and EI analysis, F1 initiated after the deposition of H1 (c. 209.5 ma), and within c. 9.4 Myr (13% of its total life) consisted of two separate segments that were 19.7 km and 19.2 km long. During this first phase of activity, it accumulated only 7% of its total throw. Approximately 28.2 Myr later, the two segments linked and the outermost tips of the newly formed fault system had propagated slightly, meaning it was now 41.3 km long. The fault had therefore reached c. 98% of its maximum length and accrued 17% of its total throw by this point (i.e. 39% of its life). Its maximum length was reached 9.4 Myr later, by which time it had accumulated 52% of its total throw. During the last 4.6 myr of the faults life, the remaining 56% of throw was accrued, and the northernmost 0.9 km and southernmost 2.9 km became inactive.

## 4.2 Fault 2

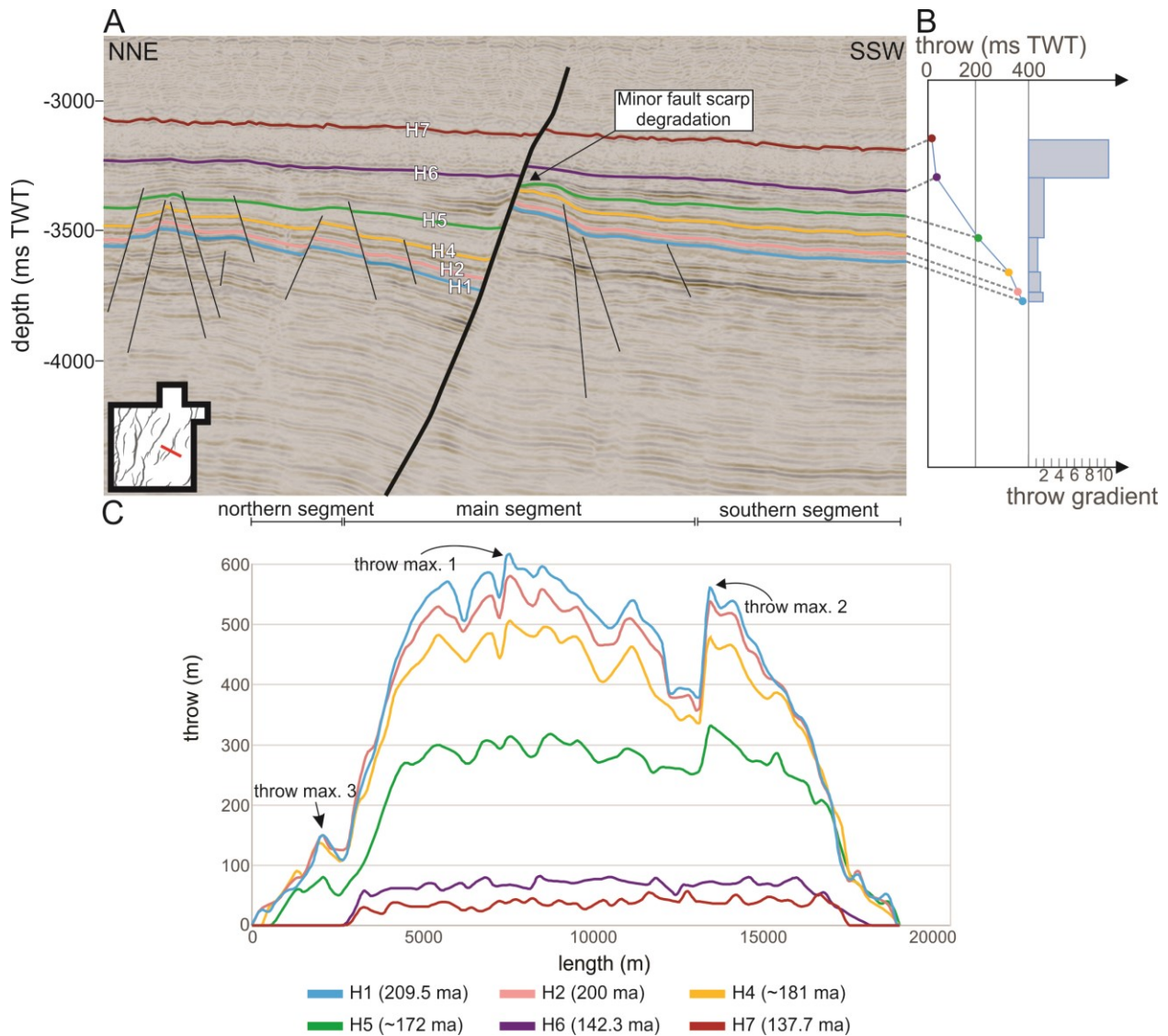


**Figure 8.** a) seismic profile illustrating F7 at its point of highest throw and its correlated throws and throw gradients, b) throw-distance plot illustrating the lateral variations in throw across each seismic unit. All throw values should be considered to be possible +20% due to decompaction (Taylor et al., 2008).



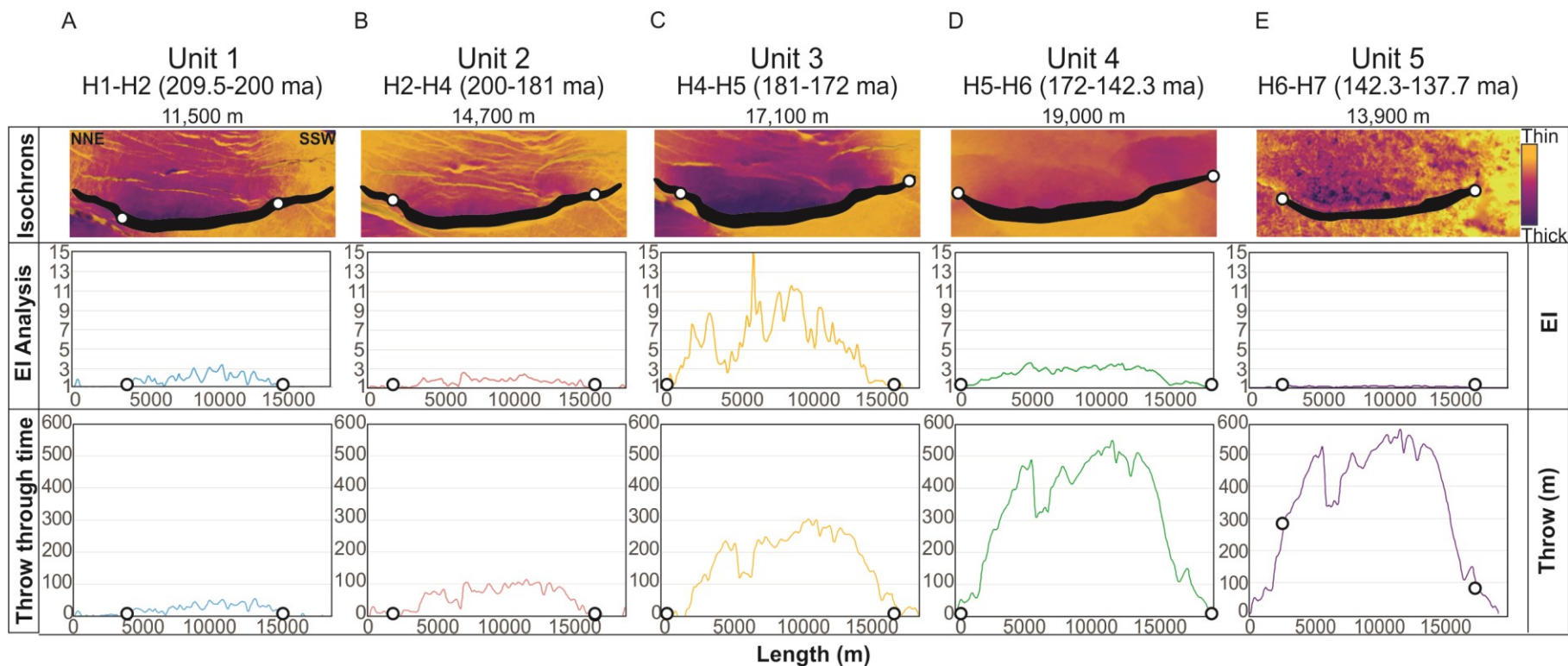


**Figure 9.** Isochrons, expansion index analysis, and throw throughout different stages of the life of Fault 7. The throw through time values are taken from displacement backstripping, which can be seen in detail in the appendix figures. White dots indicate the length of the fault at the specified interval. **a)** Isochron showing the thickness between H1 (209.5 my) and H2 (196 my), maximum throw is 55 m, and length is 11,500m, **b)** Isochron showing the thickness between H2 (196 my) and H4 (170 my), maximum throw is 116 m and length is 14,700 m, **c)** Isochron showing the thickness between H4 (170 my) and H5(162.5 my), maximum throw is 303 m and length is 17,100, **d)** Isochron showing the thickness between H5 (162.5 my) and H6 (142.3 my), maximum throw is 550 m and length is 19,000, **e)** Isochron showing the thickness between H6 (142.3 my) and H7 (137.7) my, maximum throw is 617 and length is 13,900 m. All throw values should be considered to be possible +20% due to decompaction (Taylor et al., 2008).

### 4.2.1 Observations

Fault 2 (F2) is a 19 km long, SSW-NNE-striking, WNW-dipping normal fault. F2 comprises a long (11 km) central segment that is linked at each end via abrupt bends, to shorter (3-5 km) segments (Figures 8 and 9). The upper tip-line of F1 is located in Lower Cretaceous strata, and its lower tip-line is difficult to locate due to poor seismic imaging in the pre-rift, but F1 appears to tip out deep in the study area or into the basement (Figure 4). F2 presently has three local throw maxima; a central maxima (380 ms TWT<sup>{+76}</sup>, 620 m<sup>{+124}</sup> at H1) on the main, central segment, a southern maxima (348 ms TWT<sup>{+70}</sup>, 560 m<sup>{+112}</sup> at H1) that is located along the southern fault segment, and a smaller, northern maxima (94 ms TWT<sup>{+19}</sup>, 150 m<sup>{+30}</sup> at H1) on the northern fault segment (Figure 8b). The throw maximas are separated by two throw minimas that coincide with the abrupt bends in the map-view trace of F2, where the northern and southern segments connect with the central segment (Figure 9). The main segment has an overall symmetrical throw distribution, and the northern and southern segments are skewed to the south and north respectively (Figure 8b).

There are clear wedge-shaped stratigraphic packages between H1 and H7 in the hanging wall, which thicken towards F2. Pre-H1 and post-H7 strat are isopachous (Figure 8a) EI plots show values  $\geq 1$  along a progressively longer portion of the fault from the oldest to the second youngest stratigraphic intervals (Units 1-4; Figures 9a-d). In Unit 5, the lateral tips of the fault have an EI value that is  $< 1$  (Figure 9e).

### 4.2.2 Interpretations

We see across-fault thickening between H1 and H7 (Units 1-5) in cross-section (Figure 8a) and in isochron thickness maps (Figures 9a-e), suggesting F2 was active from 209.5 to 137.7 Ma (Early Jurassic-Early Cretaceous). The fact that EI values  $\geq 1$  are limited to the central segment of the fault in Unit 1 (Figure 9a) suggests that F2 initiated here, an interpretation that is supported by the symmetry of the throw distribution on this segment (Figure 8b). The shorter southern segment is clearly present and active by Unit 3 (Figure 9c) and possibly already by Unit 2 (Figure 9b) times, as evidenced by EI values  $\geq 1$  along these segments in the corresponding interval. The throw maxima on the southern segment is skewed towards the NNE (Figure 8b), which is interpreted as a result of the mechanical interaction of the southern section with the already-existing central segment (Wilkinson et al., 2015). The northern segment is present and active by Unit 3 times (c. 28.5 myr), based on the observation of EI values  $\geq 1$  along the segment (Figure 9c). This northern segment may have simply formed due to lateral (i.e. north-northeastward) propagation of the northern tip of the central segment. However, our preferred interpretation is that it initiated as a separate segment, based on: i) the observed EI distribution within Unit 4 (i.e. the EI peak is located centrally along the SSW segment; Figure 9c); ii) the fact the throw maximum is offset to the SW of the centre of the mapped trace of the northern segment (Figure 8b); and, iii) the pronounced bend between the central and northern segments, which we infer reflects a now-breached relay ramp (Peacock & Sanderson 1994; Walsh et al., 1999). F1 reached its maximum length by the deposition of H5, or possibly sooner, as evidenced by EI  $\geq 1$  across its length during this interval. EI values drop below 1 on the lateral tips of F2 in Unit 5, which we interpret as the outer 2-2.5 km of the fault becoming inactive (Figure 9e).



In summary, according to throw backstripping and EI analysis, F2 initiated after the deposition of H1 (c. 209.5 ma), and within c. 9.4 Myr (13% of its total life) was 11.5 km long (60.5% of maximum length). During this first phase of activity, F2 only accumulated c. 13% of its total throw. Approximately 18.8 myr later, F2 had grown via tip propagation and possibly segment linkage to be 14.7 km long. At this time, the fault had reached 77.4% of maximum length and only 20% of total throw by this point (39.3% of the faults life). C. 9.4 myr later (i.e. 50.2% of the total life), the central segment of F2 grew via segment linkage to be 17.1 km long, and accumulated c. 52.4% of total throw. Its maximum length was reached within the next 29.9 myr, by which time it had accumulated c. 95.1% of its total throw. During the last 4.6 myr of the faults life, the remaining 4.9% of throw was accrued, and the northernmost 2.6 km and southernmost 2.4 km of the fault became inactive.

### 4.3 Fault 3

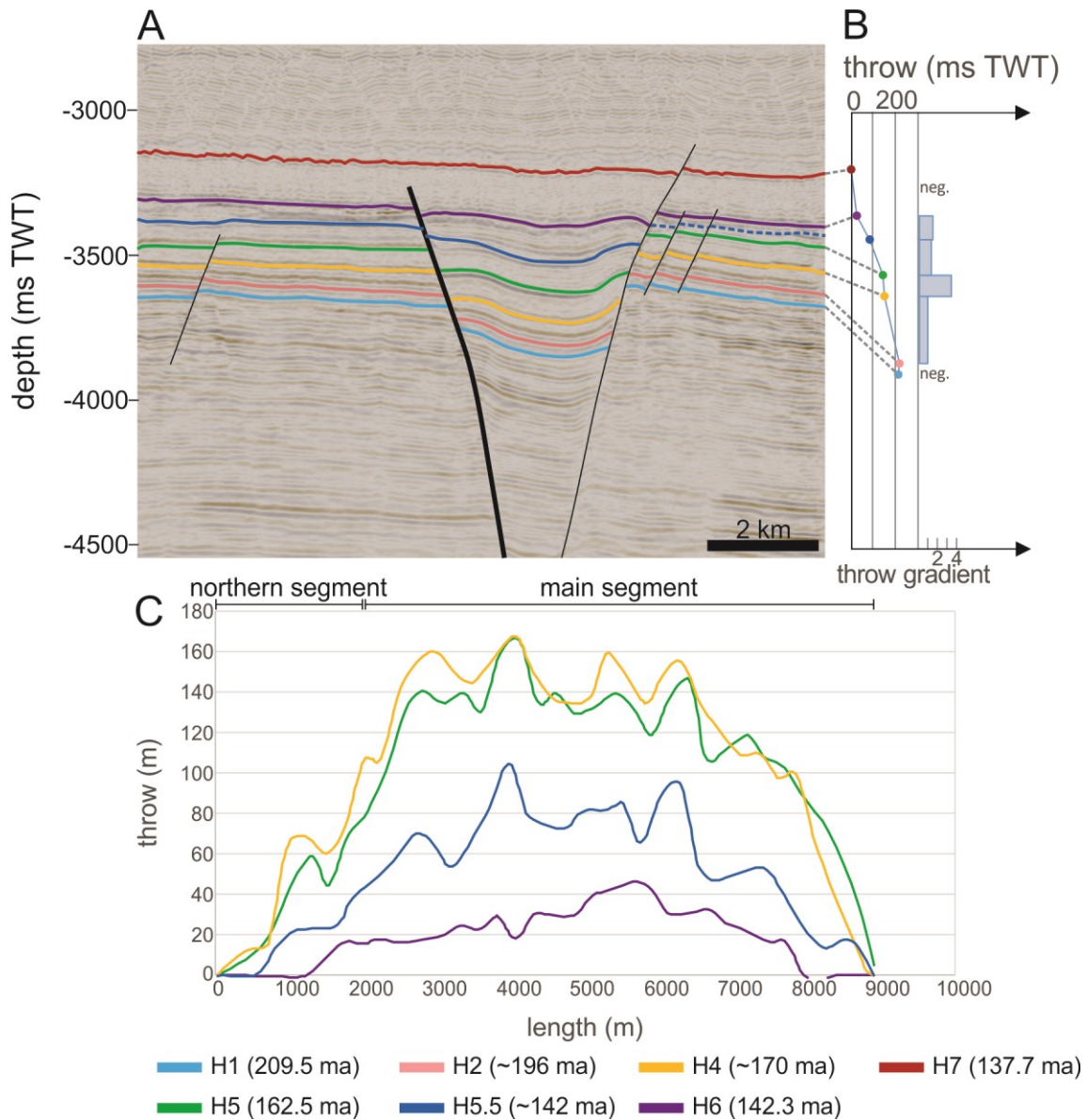


**Figure 10. a)** seismic profile illustrating F3 at its point of highest throw and its correlated throws and throw gradients, **b)** throw-distance plot illustrating the lateral variations in throw across each seismic unit. All throw values should be considered to be possible +20% due to decompaction (Taylor et al., 2008).

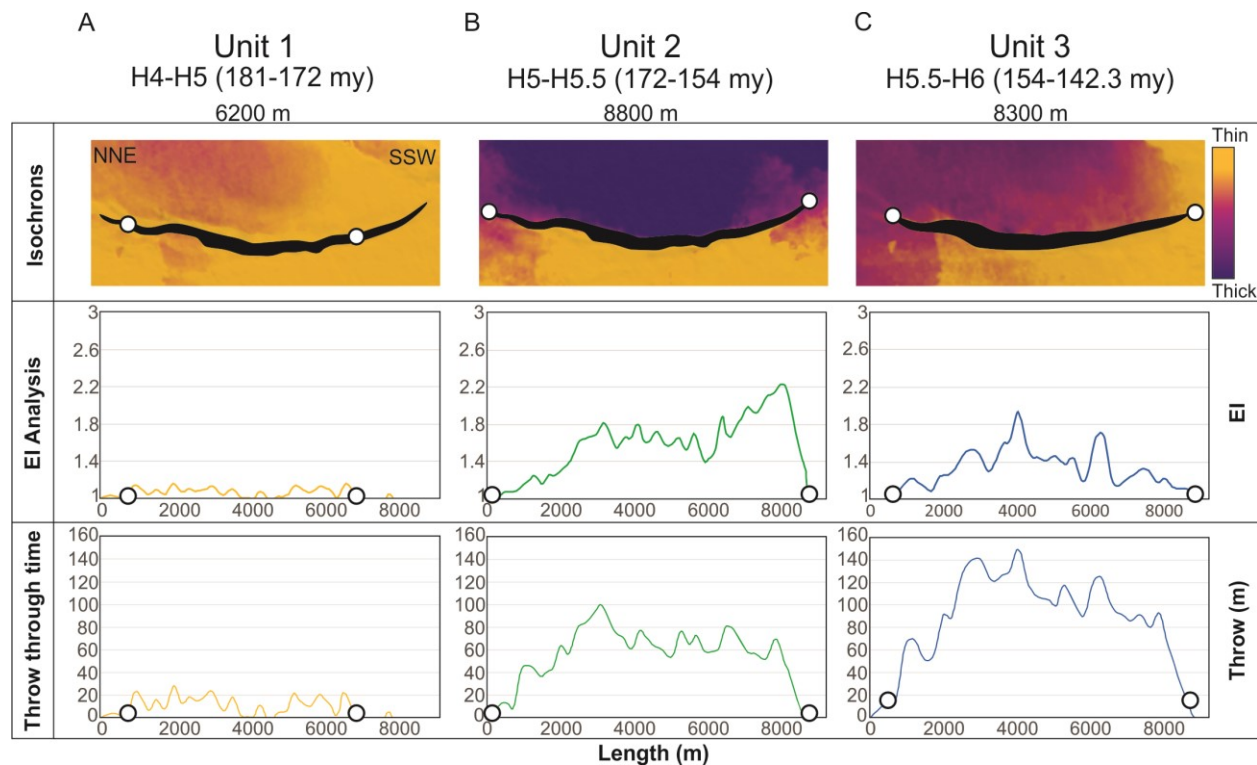


**Figure 11.** Isochrons, expansion index analysis, and throw throughout different stages of the life of F3. The throw through time values are taken from displacement backstripping, which can be seen in detail in the supplementary figures. White dots indicate the length of the fault at the specified interval. **a)** Isochron showing the thickness between H4 (170 my) and H5 (162.5 my), maximum throw is 28 m, and length is 6200 m, **b)** Isochron showing the thickness between H5 (162.5 my) and H5.5 (152 my), maximum throw is 100 m and length is 8800 m, **c)** Isochron showing the thickness between H5.5 (152 my) and H5 (142.3 my), maximum throw is 149 m and length is 8300 m. All throw values should be considered to be possible +20% due to decompaction (Taylor et al., 2008).

#### 4.3.1 Observations

Fault 3 (F3) is an 8.8 km long, NNE-SSW-striking, ESE-dipping normal fault. Its plan-view geometry consists of a slightly curved, convex-into-the-footwall segment with a small (1 km) fault branch near its northern tip (Figures 10 and 11). The upper tip-line of F1 is located in Lower Cretaceous strata, and its lower tip-line is difficult to locate due to poor seismic imaging in the pre-rift, but F1 appears to tip out deep in the study area (Figures 10). The present-day throw distribution for F3 shows two throw maxima; the main maxima (165 m<sup>{+33}</sup>, 83 ms TWT<sup>{+17}</sup> at H4) is located in the center of the main segment, with another, more minor maxima

(59 m<sup>{+12}</sup>, 37 ms TWT<sup>{+7}</sup> at H4) being associated with a possible northern segment (Figure 10b).

There are wedge-shaped stratigraphic packages between H4 and H6 in the hanging wall, which thicken towards F3. In contrast, pre-H4 and post-H6 strata are isopachous (Figure 10a). EI values are  $\geq 1$  across a progressively longer portion of the fault from Unit 1-2 (Figures 11a and 11b), and in Unit 3, the outer tips of the fault have EI values  $< 1$  (Figure 11c).

#### 4.3.2 Interpretations

We see across-fault hanging wall thickening between H4 and H6 (Units 1-3) in cross section (Fig 10a) and in isochron thickness maps (Figures 11a-c), suggesting F3 was active from c. 181 Ma to 142.3 Ma (Early Jurassic-Early Cretaceous). F3 likely initiated along its central segment during Unit 1 and reached its maximum length by the time of deposition of Unit 2 (Figure 11b); this is clearly evidenced by EI values  $\geq 1$  along the faults entire trace-length. Together with the overall bell-shaped (present) distribution of throw these EI data (Figure 11) suggest F3 grew as a single fault segment, or possibly as one large fault segment that linked with a very small segment at its northern tip. During Unit 3, EI values were  $< 1$  on the northern-most part of the fault, suggesting that the F3's northern tip became inactive (Figure 11c).

In summary, according to throw backstripping and EI analysis, F3 initiated after the deposition of H4 (c. 181 ma), and within c. 9.4 myr (24% of its total life) was c. 6.2 km long (70.5% of maximum length). During this first phase of activity, it accumulated only 18.9% of its total throw. Approximately 19.9 Myr later, F3 propagated to its maximum length of 8.8 km. The fault had therefore reached its maximum length and accrued and accrued 67% of its total throw

by this point (i.e. 75% of its life). During the last c. 4.6 myr of the faults life, the remaining 33% of throw was accrued, and the length of the fault shortened by 600 m on the NNE tip of the fault.

#### 4.4 Temporal evolution of throw and length

Most of the seven studied faults seem to have grown in three distinct stages: a lengthening stage, a throw accumulation stage, and a tip retreat stage. All of the faults have an early (i.e. first 20-30% of their lives) relatively rapid lengthening phase, during which time they reach 60-95% of their maximum length (see Figure 5a for isochrons across the study area, Figure 12a for values). Fault tips then grow slowly via tip propagation or segment linkage, reaching their maximum lengths after 57-93% of their lives (Figure 5b-c). After they reached their maximum length, all of the faults experienced a stage during which their overall at-surface trace-lengths reduced by up to 2.5 km (up to 25% of their total length) (Figures 12a-b).

Because of these shared kinematics, all of the faults studied, with the exception of F3, displayed similar temporal changes in their throw-length scaling relationship (Figures 12b and 12c). The three-stage kinematics identified above also correlate with changes in throw (Figure 12b) and slip rate (Figure 12c). For example, during the lengthening stage, slip rate is relatively low ( $3.2^{+0.68}$ -6 m/myr  $^{+1.15}$ ). During the subsequent throw accumulation stage, there was an abrupt increase in throw rate (to  $4.9^{+0.62}$ -28 m/myr  $^{+6}$ ). Throw rate decreases slightly ( $7^{+0.62}$ -20 $^{+4.8}$  m/myr) as the faults die. It should be noted that the throw rate during the first half of the faults life (until deposition of H5) is likely underestimated due to the basin being somewhat sediment starved during this period. A higher slip rate would mean the time difference between the lengthening and throw accumulation stages is smaller.

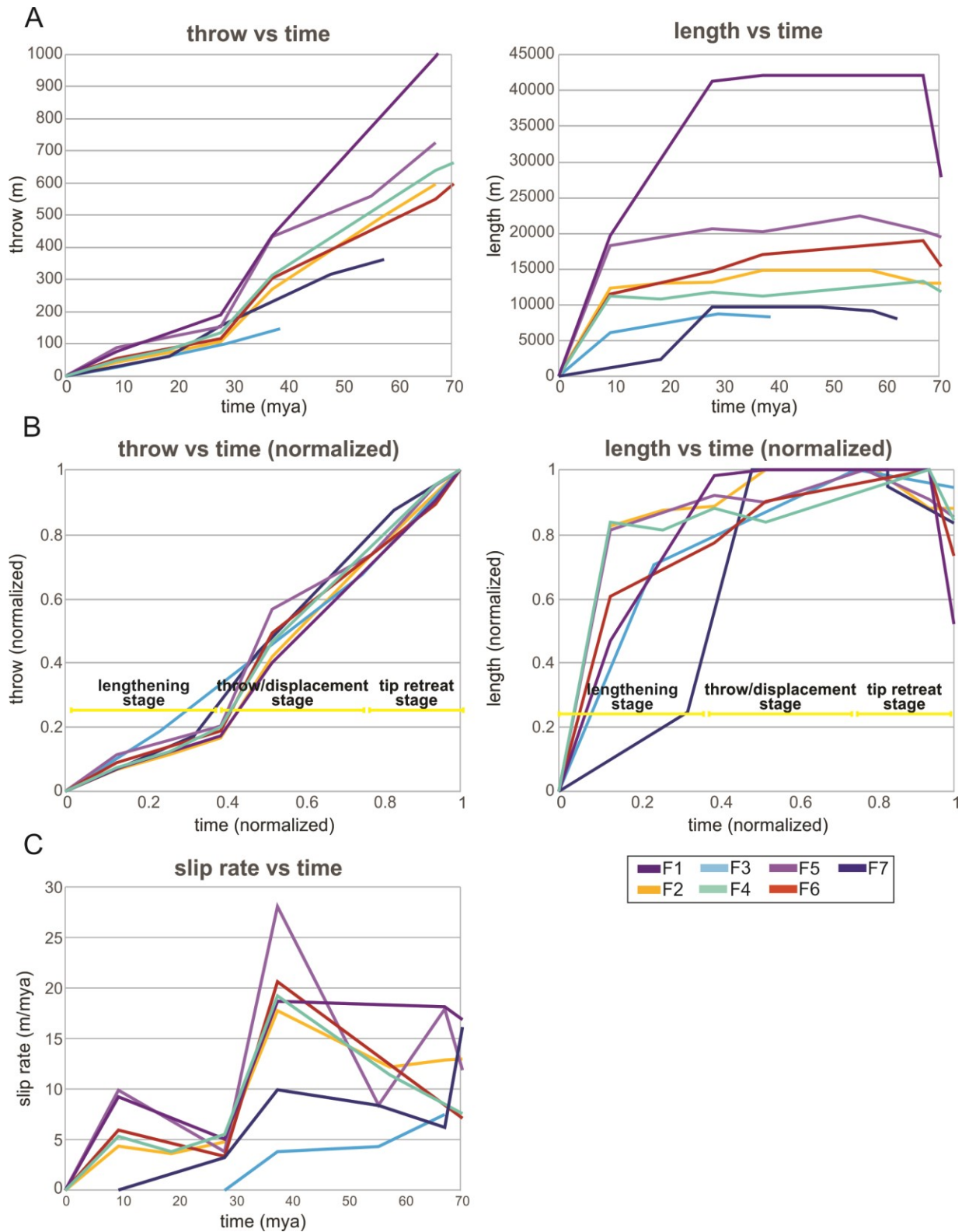


**Figure 12.** throw and lengthening through time for F1-8 in time and normalized. The lengthening, throw/displacement, and tip retreat stages of faulting are labelled in the normalized graphs. All throw values should be considered to be possible +20% due to decompaction (Taylor et al., 2008).

## **5 Discussion**

### **5.1 Implications for fault growth models**

Our study identifies three key stages of fault growth. First, there is an initial lengthening stage (Figure 13a); all of the faults reach 60-95% of their maximum length within the first 20-30% of their lives. Maximum length is later reached via tip propagation or segment linkage. Second, there is then a throw accumulation stage (Figure 13b) that lasts from ~30-75% of the faults life; during this time, faults lengthen very little and experience an increased slip rate. Third, the tip retreat stage, (Figure 13c and 13d) that lasts for the final 25% of the faults life during which the faults experience tip-line retreat, and throw is partitioned towards the center of the fault. Our findings are generally consistent with the model of Rotevatn et al. (2019), but we suggest two important amendments. First, the fault maximum length is not always reached during the initial lengthening stage; i.e our results demonstrate that, while the bulk of lengthening happens relatively quickly, 5-40% can subsequently occur during lateral tip propagation and/or segment linkage. Variations in when the fault reaches its maximum length is likely controlled by whether a fault links with a nearby segment or not, a process perhaps dictated by the ability of the faults to breach the intervening relay. Second, there could be a stage of tip retreat at the end of the faults' life (Figures 13c and 13d); i.e. every fault in this study underwent tip retreat, suggesting that this may be a generic aspect of fault evolution than currently appreciated, and that it should thus be included in fault evolution models.



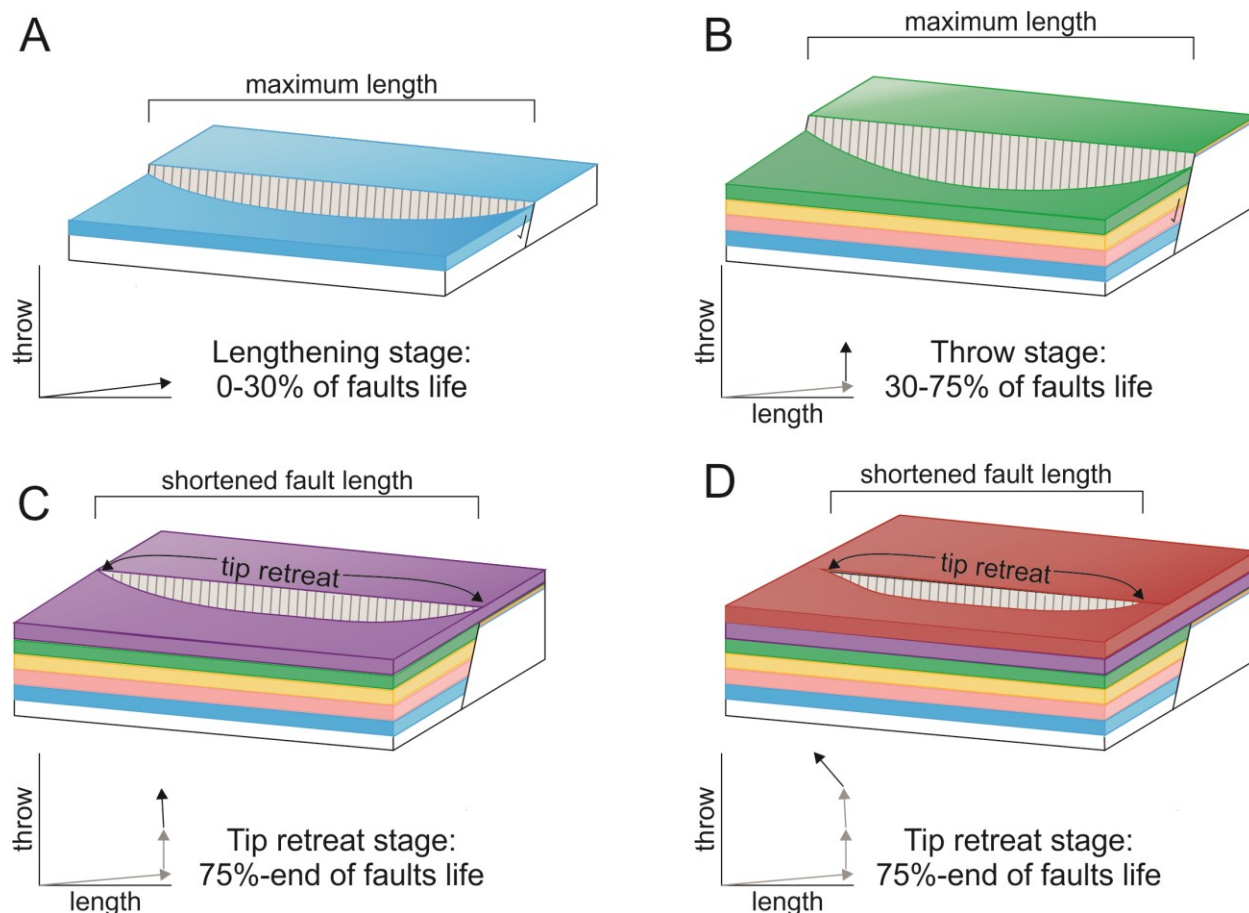


**Figure 13.** Schematic models showing the phases of fault growth. **a)** Fault lengthening stage, when faults establish their near-maximum length within the first 30% of their life **b)** Fault throw accrual stage, where faults have already reached their maximum length, and throw rate increases **c)** the beginning of the tip retreat stage, where the tips of the fault become inactive and **d)** the continuation of the tip retreat stage, where the active fault trace line is progressively shorter

In previous work on normal fault growth models, slip rate is often not quantified. Some work has shown that there is some variability in slip rate on a scale of thousands of years, but that slip rates even out on a longer temporal scale (greater than 300 kry) or spatial length scale (e.g. entire fault system) (Mouslopoulou et al., 2009; Nicol et al., 2006). However, our work has shown slip rates that vary significantly on a scale of millions of years, ranging between 3.8 m/myr and 28 m/myr. Long-term fluctuations in slip rate like we see could be a result of changes in regional strain rate (Mouslopoulou et al., 2009) or fault interactions (Cowie & Roberts, 2001),



however it is possible that further research needs to be done to see how slip rates could vary in different faults over long periods of time.

Our results also allow us to further refine fault growth models by considering how slip rate varies with time. Previous work shows slip rate is highly variable on timescales of a few thousand years, but that these rates are less variable when viewed on a longer temporal- (i.e. >300 kry) or spatial-scales (i.e. an entire fault system) (Mouslopoulou et al., 2009; Nicol et al., 2006). However, our work has shown that slip rates can vary significantly (3.8-28 m/Myr) on temporal-scales spanning several million years. These long-term fluctuations in slip rate may reflect changes in regional strain rate (Mouslopoulou et al., 2009), or the observed accelerated slip rates could be a result of strain localization onto larger faults (Cowie & Roberts, 2001; Gupta et al., 1998).

Additionally, the ‘final’ length of a fault is often mentioned in normal fault databases (Bailey et al., 2005; Cowie & Schultz 1992; Kim & Sanderson, 2005; Schultz & Fossen, 2002; Walsh et al., 1998). We have demonstrated that because some faults may experience a stage of tip retreat at the end of their active lives, their ‘final length’ may be up to 25% smaller than their ‘maximum length’, which could affect displacement/length plots in global normal fault databases. Thus, it is important to extract the displacement/length at the base of the pre-rift, given this records the maximum extensional strain.

## **5.2 The role of tip retreat**

Fault tip retreat is present on one or both tips of all of the faults in our study. This process has, however, only very rarely been described. Meyer et al., (2002) note a stage of tip retreat on Tertiary normal faults in the Vulcan Sub-basin, NW Shelf, Australia. The reasons why fault tips might retreat may have been overlooked because of a historical focus on how normal faults grow

as opposed to how they die, and/or because high-quality, age-constrained seismic reflection data, with numerous mappable horizons within fault-related growth strata, are not available. Noting that tip retreat could be a fundamental part of how normal faults evolve is important when trying to understand seismic hazard in areas of active continental extension. For example, earthquake-scaling relationships might suggest that as the active trace-length of a fault decreases, the potential magnitude of earthquakes that could be hosted on that fault may also decrease (Coppersmith & Wells 1994). However, the trace-length of large, mature faults entering the late, tip-retreat stage of their evolution, likely represents only a small portion of the fault surface; these faults could thus generate significantly larger earthquakes than predicted by scaling-relationships. Current structural models for seismic hazard analysis in areas of extensional tectonics do not currently, but maybe should, take fault age or maturity into account (e.g. Manighetti et al., 2007; Wallace, 1970).

All of the studied faults decreased in length (by up to 2.5 km, or 25% of their trace-length) during the last 14 million years (25%) of their lives by retreat of one or both of their lateral tips. This could be explained by two hypotheses. The first hypothesis is that the faults are experiencing a late-stage of *true* tip retreat; i.e. strain becomes localized near the fault centre, leading to progressively shorter surface trace. We would expect that fault surface ruptures shorten as the fault gets closer to death (Figure 14a). An alternate hypothesis is that tip-line retreat is only *apparent* and is related to the faults having an elliptical geometry during the later stages of faulting, due to it having a plunging upper tip-line (i.e. during deposition of H5-7; Figure 14b). In this scenario, the fault would have intersected the free-surface along progressively shorter trace-lengths, with the fault tips being blind (Figure 13b). An increase in sediment accumulation rate relative to fault slip rate could drive this progression. The fault

geometries associated with both hypotheses would look similar in seismic data (cf Figures 14a and 14b).

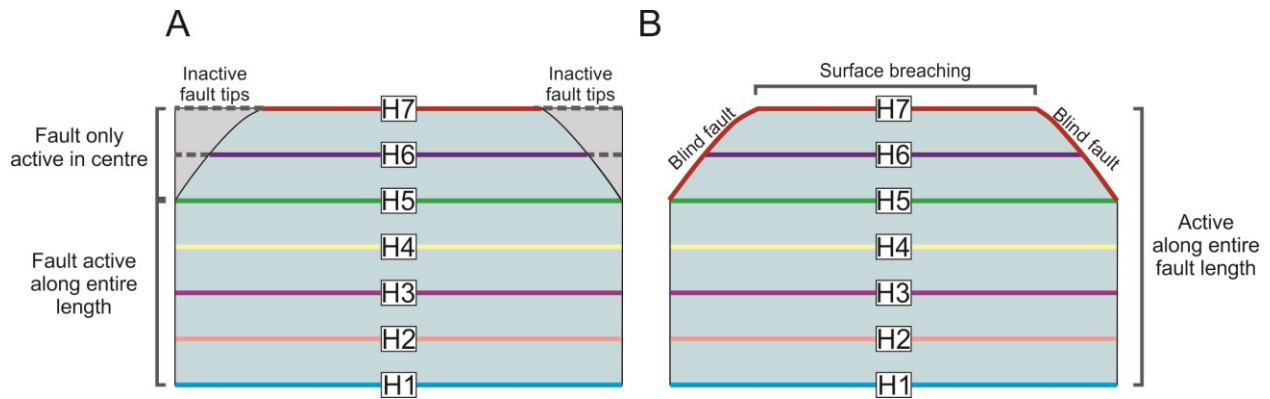


**Figure 14.** Schematics showing a two possibilities for the apparent tip line retreat in this study. Fault planes along dip are shown, and colored lines indicate the active length of the fault at the time of the deposition of the associated horizons (H1-7). **a)** Fault length remains constant from H1-5, and becomes active a progressively shorter distances across H6 and H7, which can be interpreted as lateral tip retreat. **b)** the fault remains active across the entire length of the fault, but in the later stages of faulting (H6-7) the fault only breaches the surface in the centre of the fault, and the fault tips remain active at depth, acting as blind faults.

We argue that we are seeing true fault tip retreat because if retreat was only apparent and related to the faults elliptical shape, we would expect vertical throw gradients across the horizons to be similar to those encountered on blind normal faults (Childs et al., 2003; Meyer et al., 2002; Walsh & Watterson 1988). For a blind fault, only modest strain can be accommodated by the rock volume without upward tip propagation. In the case of the upper tip of a blind fault, a maximum vertical displacement gradient of  $<0.1$  is typical (Baudon & Cartwright, 2009; Childs et al., 2003; Meyer et al., 2002; Walsh & Watterson, 1998). We measured the maximum vertical displacement gradients between H6 and H7 in the centre of the faults and found values between 2-7 (Figures 6b, 8b, and 10b), more than an order-of-magnitude higher than that typically found for blind faults (Walsh & Watterson, 1988) (Figure 13). Such high vertical displacement gradients suggest that the *entire length* of the upper tip-line must have intersected the free-

surface (Baudon & Cartwright, 2009; Childs et al., 2003; Meyer et al., 2002), and that a portion of the fault had become inactive during the later stages of the faults life, before the deposition of H6 and H7.

When verifying that the tip retreat we see is real, it is important to ensure that the faults are not sediment-starved during the latter stages of their development (post-Jurassic). A reported example of possible tip retreat comes from the East African Rift (Morley, 2002); however, in this case it is possible that the faults became inactive earlier than assumed, and what appears to be tip retreat is only (passive) sediment filling of a starved basin. In our study, we argue the faults were not sediment-starved at the end of their lives (Berriasian-Hauterivian), given appreciable amounts of sediment were deposited in the footwall of the faults during deposition of H5 to H7 (Figures 6a, 7a and 9a).

## **6 Conclusions**

The majority of the studied faults have three distinct stages of fault evolution. During the first stage, the “lengthening stage”, the faults accumulate at least between 60-95% of their final length and accrues between 10-20% of throw. This stage lasts for up to 30% of the faults’ life. The second stage, termed the “throw stage”, fault throw rate increases, and the remainder of maximum fault length is reached. We also suggest that there could be a third stage of fault growth added to previous fault models, the tip retreat stage, where the active trace line of the fault decreases by up to 25% and throw continues to be accrued. More evidence is needed to determine how prevalent tip retreat is, but it could be an important part of late stage fault growth and should be included in future fault growth models.

## Acknowledgments

We thank the Imperial College for providing Bailey Lathrop with the Presidential scholarship to fund her PhD research. We thank Geoscience Australia for making all of the data used in this study publically available, which can be found at <https://www.ga.gov.au/nopims>. We thank Schlumberger for providing access to Petrel software. We also thank the Imperial College Basins Research Group (BRG) for their input and help throughout this research, and many colleagues with whom we have had beneficial conversations with at EGU and TSG conferences.

## References

- Bailey, W. R., Walsh, J. J., & Manzocchi, T. (2005). Fault populations, strain distribution and basement fault reactivation in the East Pennines Coalfield, UK. *Journal of Structural Geology*, 27, 913–928. <https://doi.org/10.1016/j.jsg.2004.10.014>
- Baudon, C., & Cartwright, J. A. (2008). 3D seismic characterisation of an array of blind normal faults in the Levant Basin, Eastern Mediterranean. *Journal of Structural Geology*, 30(6), 746–760. <https://doi.org/10.1016/j.jsg.2007.12.008>
- Bilal, A., McClay, K. E. N., & Scarselli, N. (2020). Fault-scarp degradation in the central Exmouth Plateau, North West Shelf, Australia. *Geological Society, London, Special Publications*, 476(1), 231–257.
- Bouroullec, R., Cartwright, J. A., Johnson, H. D., Lansigu, C., Quemener, J., & Savanier, D. (2004). Syndepositional faulting in the Gres d'Annot Formation, SE France : high-resolution kinematic analysis and stratigraphic response to growth faulting. *Geological Society Special Publication*, 221, 241–265.

- Brown, A. R. (2011). Interpretation of Three-Dimensional Seismic Data. *AAPG Memoir 42, /SEG Investigation in Geophysics, 9(42)*.
- Cartwright, J. A., & Dewhurst, D. N. (1998). Layer-bound compaction faults in fine-grained sediments. *GSA Bulletin, 110(10)*, 1242–1257.
- Cartwright, J. A., Trudgill, B. D., & Mansfield, C. S. (1995). Fault growth by segment linkage: an explanation for scatter in maximum displacement and trace length data from the Canyonlands Grabens of SE Utah. *Journal of Structural Geology, 17(9)*, 1319–1326.  
[https://doi.org/10.1016/0191-8141\(95\)00033-A](https://doi.org/10.1016/0191-8141(95)00033-A)
- Chapman, T. J., & Meneilly, A. W. (1991). The displacement patterns associated with a reverse-reactivated, normal growth fault. *Geological Society Special Publication, 56*, 183–191.
- Childs, C., Holdsworth, R. E., Jackson, C. A.-L., Manzocchi, T., Walsh, J. J., & Yielding, G. (2017). Introduction to the geometry and growth of normal faults. *Geological Society, London, Special Publications, SP439.23*. <https://doi.org/10.1144/SP439.24>
- Childs, C., Nicol, A., Walsh, J. J., & Watterson, J. (2003). The growth and propagation of synsedimentary faults. *File:///C:/Users/Balat/OneDrive - Imperial College London/Papers/Aapg\_1987\_0071\_0008\_0925.Pdf, 8141(May)*.  
[https://doi.org/10.1016/S0191-8141\(02\)00054-8](https://doi.org/10.1016/S0191-8141(02)00054-8)
- Cowie, P. A., & Scholz, C. H. (1992). Displacement-length scaling relationship for faults: data synthesis and discussion. *Journal of Structural Geology, 14(10)*, 1149–1156.  
[https://doi.org/10.1016/0191-8141\(92\)90066-6](https://doi.org/10.1016/0191-8141(92)90066-6)

- Dawers, N. H., Anders, M. H., & Scholz, C. H. (1993). Growth of normal faults: displacement-length scaling. *Geology*. [https://doi.org/10.1130/0091-7613\(1993\)021<1107:GONFDL>2.3.CO;2](https://doi.org/10.1130/0091-7613(1993)021<1107:GONFDL>2.3.CO;2)
- Ford, M., Hemelsdaël, R., Mancini, M., & Palyvos, N. (2016). Rift migration and lateral propagation: evolution of normal faults and sediment-routing systems of the western Corinth rift (Greece). *Geological Society, London, Special Publications 439*, (April 2012), SP439.15. <https://doi.org/10.1144/SP439.15>
- Fossen, H., & Rotevatn, A. (2016). Fault linkage and relay structures in extensional settings-A review. *Earth-Science Reviews*, *154*, 14–28. <https://doi.org/10.1016/j.earscirev.2015.11.014>
- Freitag, U. A., Sanderson, D. J., Lonergan, L., & Bevan, T. G. (2017). Comparison of upwards splaying and upwards merging segmented normal faults. *Journal of Structural Geology*, *Volume 100*(2017), 1–11. <https://doi.org/10.1016/j.jsg.2017.05.005>
- Gupta, A., & Scholz, C. H. (1998). Utility of elastic models in predicting fault displacement fields. *Journal of Geophysical Research*, *103*, 823–834.
- Henstra, G. A., Rotevatn, A., & Gawthorpe, R. L. (2015). Evolution of a major segmented normal fault during multiphase rifting : The origin of plan-view zigzag geometry. *Journal of Structural Geology*, *74*, 45–63.
- Jackson, C. A.-L., Bell, R. E., Rotevatn, A., & Tvedt, A. B. M. (2017). Techniques to determine the kinematics of synsedimentary normal faults and implications for fault growth models.

*Geological Society, London, Special Publications*, SP439.22.

<https://doi.org/10.1144/SP439.22>

Jackson, C. A. L., & Rotevatn, A. (2013). 3D seismic analysis of the structure and evolution of a salt-influenced normal fault zone: A test of competing fault growth models. *Journal of Structural Geology*, 54, 215–234. <https://doi.org/10.1016/j.jsg.2013.06.012>

Kim, Y. S., & Sanderson, D. J. (2005). The relationship between displacement and length of faults: A review. *Earth-Science Reviews*, 68(3–4), 317–334.

<https://doi.org/10.1016/j.earscirev.2004.06.003>

Longley, I. M., Buessenschuett, C., Clydsdale, L., Cubitt, C. J., Davis, C. J., Johnson, R. C., ... Thompson, N. B. (2002). The North West Shelf of Australia - A Woodside Perspective. *Proceedings of the Petroleum Exploration Society of Australia Symposium*, 27–88.

Manighetti, I., Campillo, M., Bouley, S., & Cotton, F. (2007). Earthquake scaling, fault segmentation, and structural maturity. *Earth and Planetary Science Letters*, 253, 429–438.

<https://doi.org/10.1016/j.epsl.2006.11.004>

Marshall, N. G., & Lang, S. C. (2013). A New Sequence Stratigraphic Framework for the North West Shelf, Australia. *The Sedimentary Basins of Western Australia 4: Proceedings PESA Symposium*, 1–32.

Meyer, V., Nicol, A., Childs, C., Walsh, J. J., & Watterson, J. (2002). Progressive localisation of strain during the evolution of a normal fault population. *Journal of Structural Geology*, 24(8), 1215–1231. [https://doi.org/10.1016/S0191-8141\(01\)00104-3](https://doi.org/10.1016/S0191-8141(01)00104-3)



Morley, C. K. (2002). Evolution of large normal faults: Evidence from seismic reflection data.

*AAPG Bulletin*, 86(6), 961–978. <https://doi.org/10.1306/61EEDBFC-173E-11D7->

8645000102C1865D

Mouslopoulou, V., Walsh, J. J., & Nicol, A. (2009). Fault displacement rates on a range of timescales. *Earth and Planetary Science Letters*, 278(3–4), 186–197.

<https://doi.org/10.1016/j.epsl.2008.11.031>

Nicol, A., Childs, C., Walsh, J. J., Manzcchi, T., Scho, M. P. J., Hutt, L., ... Group, F. A.

(2016). Interactions and growth of faults in an outcrop-scale system. *The Geological Society of London Special Publication*, 439, 23–39. <https://doi.org/10.1144/SP439.9>

Nicol, A., Walsh, J. J., Berryman, K., & Villamor, P. (2006). Interdependence of fault

displacement rates and paleoearthquakes in an active rift. *Geology*, 34(10), 865–868.

<https://doi.org/10.1130/G22335.1>

Nugraha, H. D., Hodgson, D. M., Reeve, M. T., Jackson, C. A. L., & Johnson, H. D. (2019).

Tectonic and oceanographic process interactions archived in Late Cretaceous to Present deep - marine stratigraphy on the Exmouth Plateau , offshore NW Australia. *Basin*

*Research*, 31(2018), 405–430. <https://doi.org/10.1111/bre.12328>

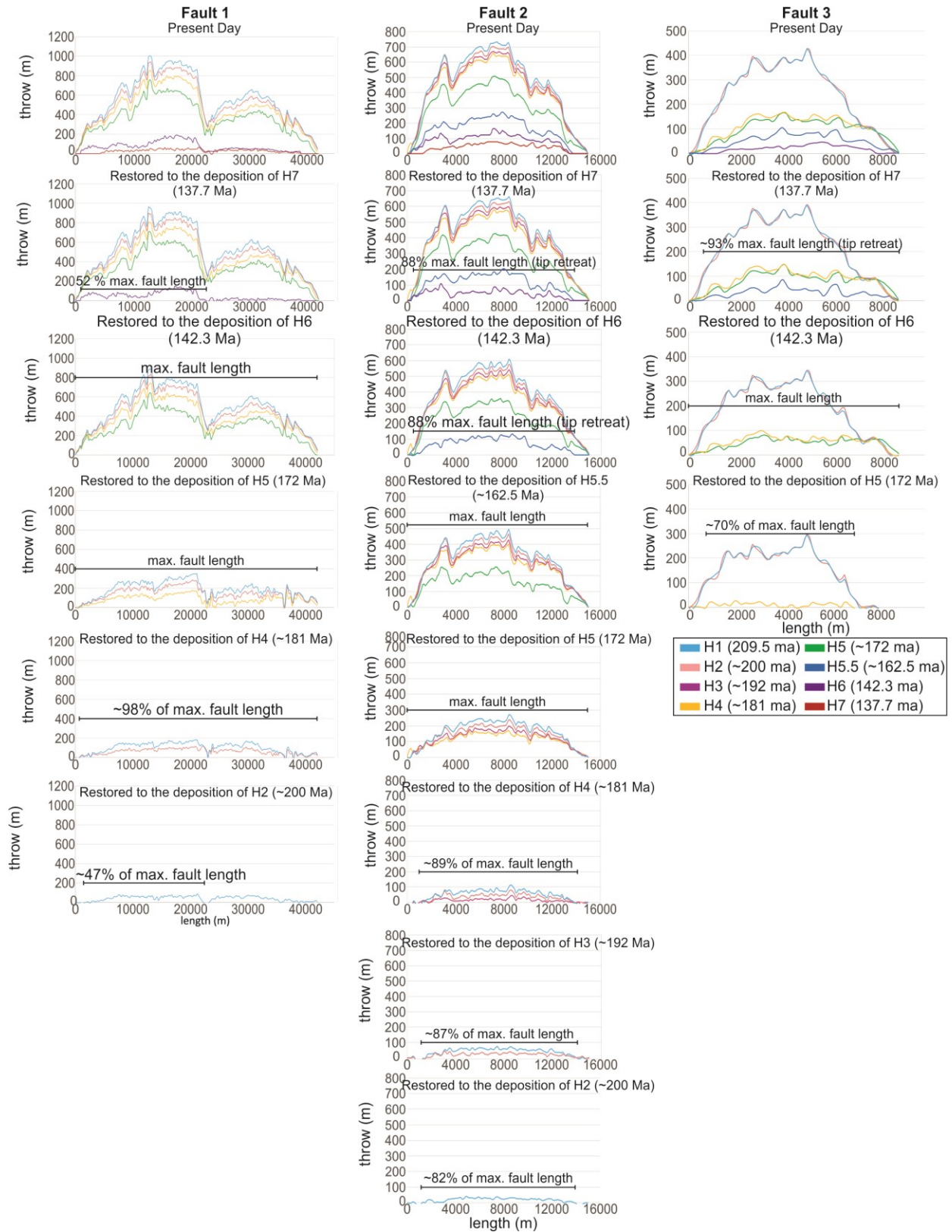
Pan, S., Bell, R. E., Jackson, C. A. L., Nailboff, J. (2020). An updated fault growth model

constrained by seismic array-scale observations. *In Prep*.

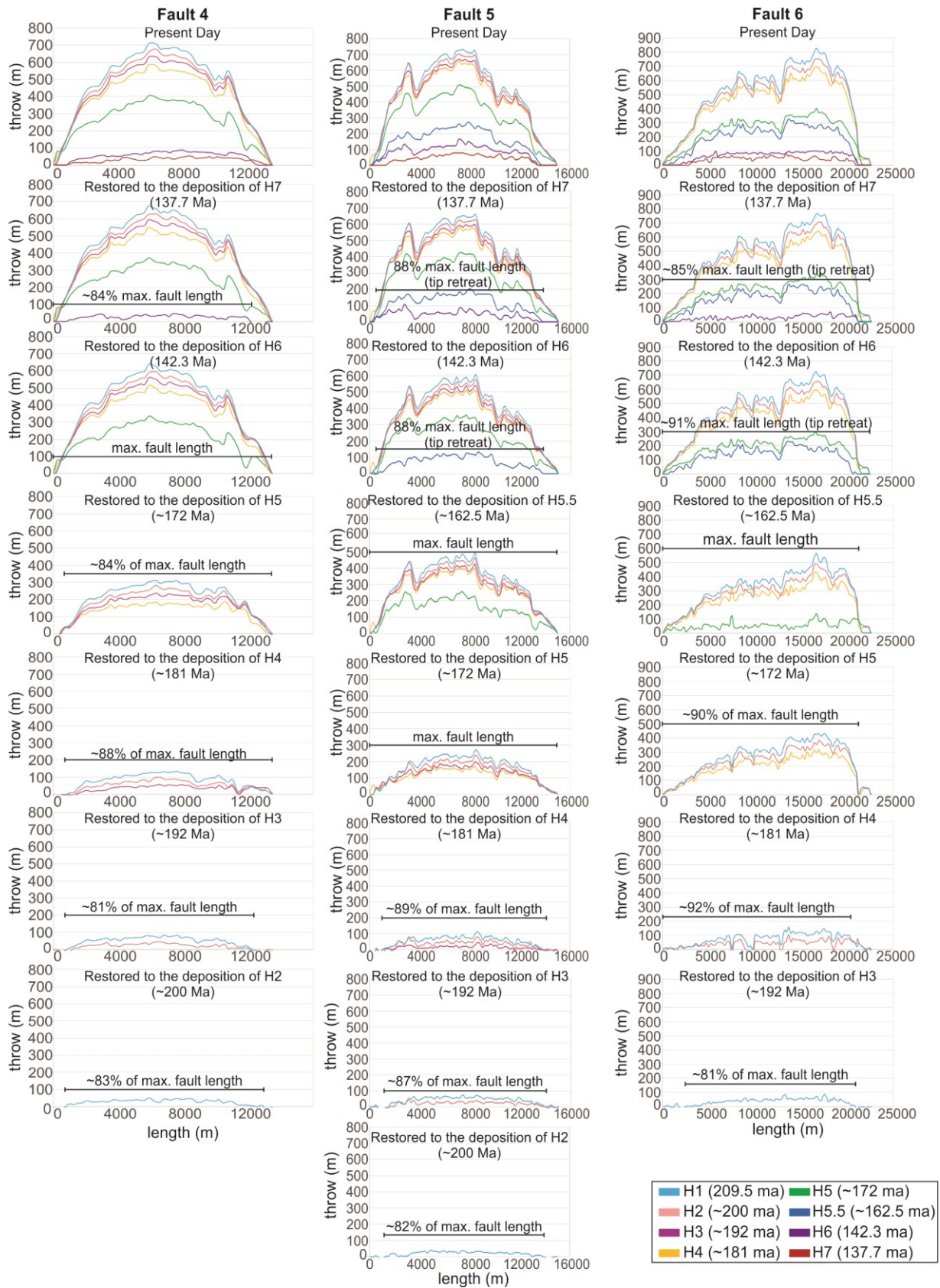
- Rotevatn, A., Jackson, C. A. L., Tvedt, A. B. M., Bell, R. E., & Blækkan, I. (2018). How do normal faults grow? *Journal of Structural Geology*, (August), 0–1.  
<https://doi.org/10.1016/j.jsg.2018.08.005>
- Schultz, R. A., & Fossen, H. (2002). Displacement-length scaling in three dimensions: The importance of aspect ratio and application to deformation bands. *Journal of Structural Geology*, 24(9), 1389–1411. [https://doi.org/10.1016/S0191-8141\(01\)00146-8](https://doi.org/10.1016/S0191-8141(01)00146-8)
- Stagg, H. M. J., Colwel, J. B., Direen, N. G., Brien, P. E. O., Bernardel, G., Borissova, I., ... Ishirara, T. (2005). Geology of the continental margin of Enderby and Mac . Robertson Lands , East Antarctica : Insights from a regional data set. *Marine Geophysical Researches*, 25, 183–219. <https://doi.org/10.1007/s11001-005-1316-1>
- Stagg, H. M. J., & Colwelp, J. B. (1994). The Structural Foundations of the Northern Carnarvon Basin . *The Sedimentary Basins of Western Australia: Proceedings of Petroleum Exploration Society of Australia Symposium, Perth*, 349–372.
- Thorsen, C. E. (1963). Age of growth faulting in Southeast Louisiana. *Gulf Coast Association of Geological Societies Transactions*, 3, 103–110.
- Tindale, K., Newell, N., Keall, J., & Smith, N. (1998). Structural Evolution and Charge History of the Exmouth Sub-basin, Northern Carnarvon Basin, Western Australia. *The Sedimentary Basins of Western Australia 2: Proceedings of Petroleum Exploration Society of Australia Symposium*.

- Tvedt, A. B. M., Rotevatn, A., & Jackson, C. A. L. (2016). Supra-salt normal fault growth during the rise and fall of a diapir: Perspectives from 3D seismic reflection data, Norwegian North Sea. *Journal of Structural Geology*, *91*, 1–26. <https://doi.org/10.1016/j.jsg.2016.08.001>
- Wallace, R. E. (1970). Earthquake Recurrence Intervals on the San Andreas Fault. *Geological Society of America Bulletin*, *81*, 2875–2890.
- Walsh, J. J., & Watterson, J. (1988). Analysis of the relationship between displacements and dimensions of faults. *Journal of Structural Geology*, *10*(3), 239–247.  
[https://doi.org/10.1016/0191-8141\(88\)90057-0](https://doi.org/10.1016/0191-8141(88)90057-0)
- Wells, D. L., & Coppersmith, K. J. (1994). New Empirical Relationships among Magnitude, Rupture Length, Rupture Width, Rupture Area, and Surface Displacement. *Bulletin of the Seismological Society of America*, *84*(4), 974–1002.
- Wilson, P., Elliott, G. M., Gawthorpe, R. L., Jackson, C. A., Michelsen, L., & Sharp, I. R. (2013). Geometry and segmentation of an evaporite-detached normal fault array : 3D seismic analysis of the southern Bremstein Fault Complex , offshore mid-Norway. *Journal of Structural Geology*, *51*, 74–91. <https://doi.org/10.1016/j.jsg.2013.03.005>

## Appendix

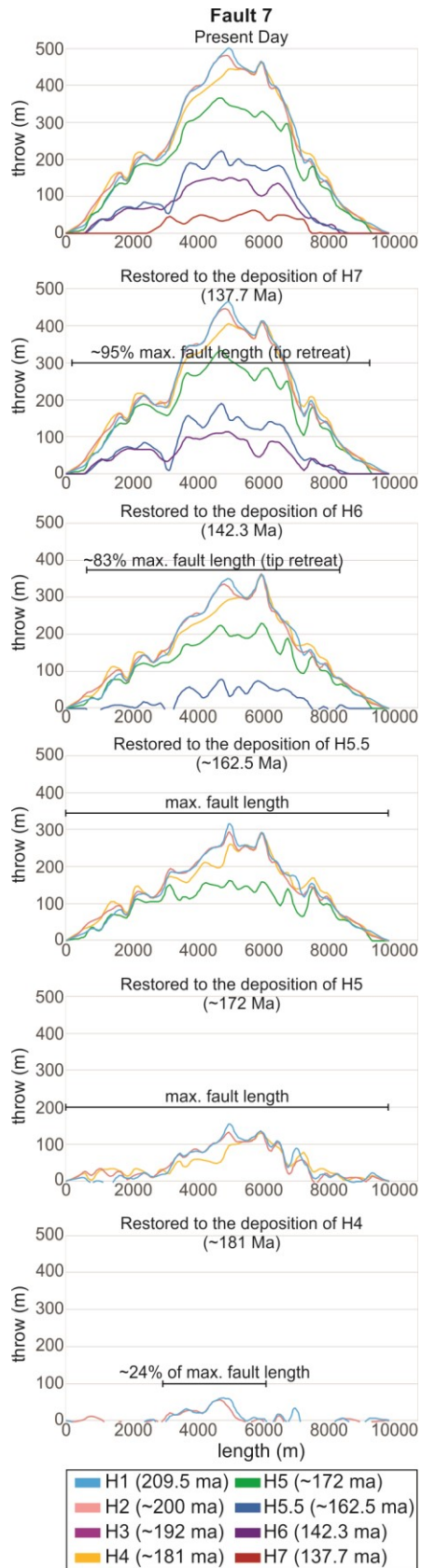


Appendix figure 1. throw backstripping faults 1-3

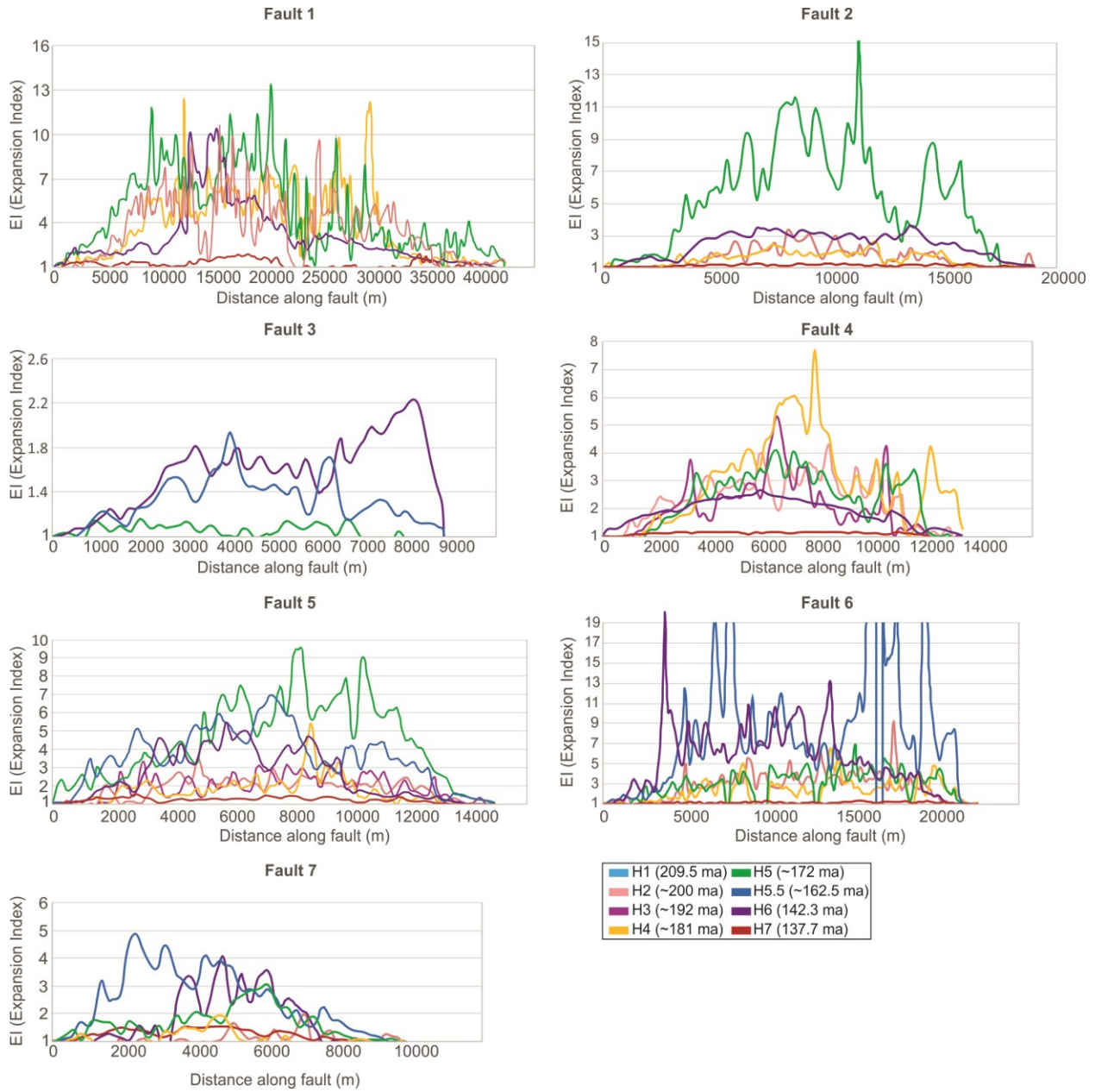


**Appendix figure 2.** Throw backstripping faults 4-6



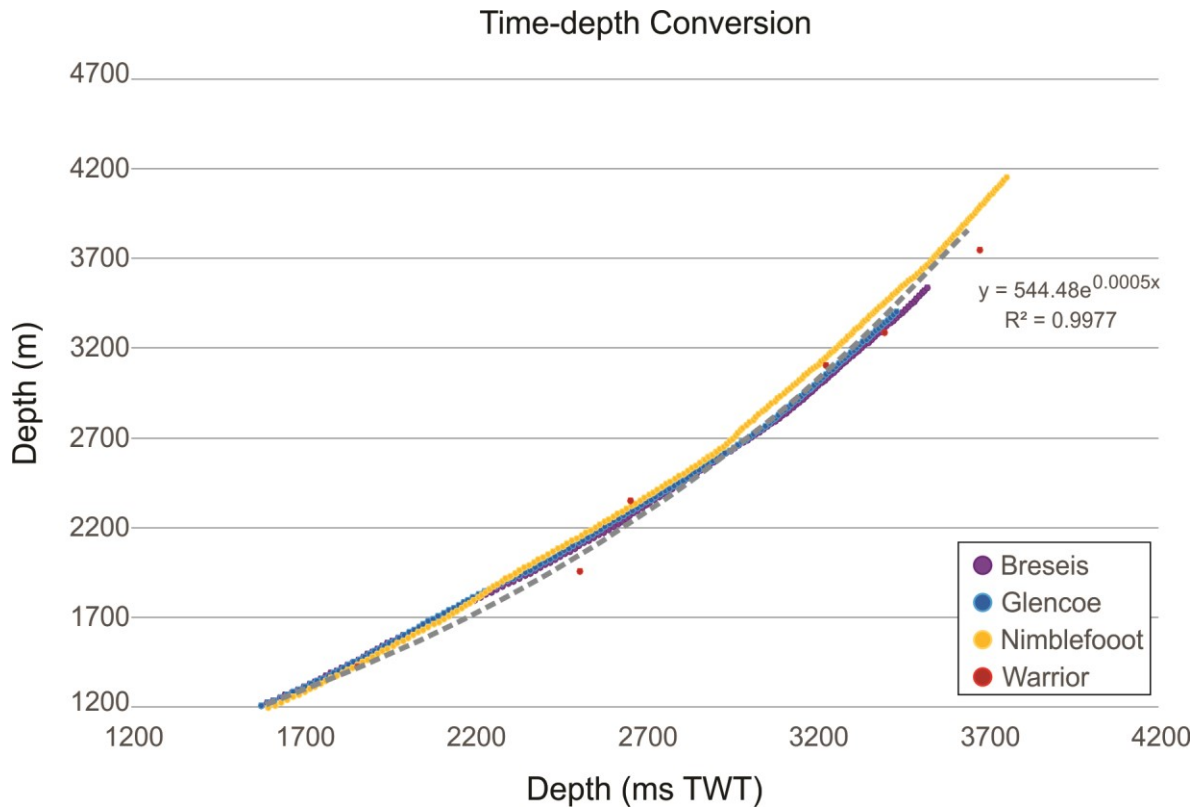


**Appendix figure 3.** Throw backstripping fault 7



**Appendix figure 4.** EI Analysis for faults 1-7





**Appendix figure 5.** Time-depth conversion for the 4 four wells in the study area: Breseis-1, Glencoe-1, Nimblefoot-1, and Warrior-1.